

Master's thesis

Performance and
optimization studies on the
time-over-threshold readout of the
multi-PMT optical module for future
IceCube extensions

Untersuchungen zu Performance und Optimierung der
time-over-threshold Auslese des multi-PMT optischen Moduls
für zukünftige IceCube Erweiterungen

submitted by
Daniel Guderian

— January 2018 —

“I don’t like quotes. But it was in the template...”

-Martin Unland

Contents

1	The neutrino as a messenger from the high-energy universe	3
1.1	Neutrinos in the Standard Model of particle physics	3
1.2	Messengers from the high-energy universe	5
1.3	Neutrino interactions	8
2	Detecting neutrinos with IceCube and future extensions	11
2.1	The detection principle in large volume experiments	11
2.2	The IceCube detector and the Digital Optical Module	12
2.3	First observations of astrophysical high-energy neutrinos	16
2.4	Future IceCube extensions and the mDOM	18
3	Pulse reconstruction and simulation software	23
3.1	The IceTray framework and pulse reconstruction in IceCube	23
3.1.1	Deconvolution of the DOM response to photons	24
3.2	Standalone python simulation program	26
3.2.1	The time-over-threshold algorithm	27
3.3	Incorporating the ToT algorithm into IceTray to analyze real data	29
4	Optimizing threshold setups for single photoelectron pulses	33
4.1	Parameter distributions and analysis	33
4.1.1	Parameter behavior for large numbers of iterations	38
4.2	Method and results of optimization	39
4.2.1	Cuts in time and charge and characteristics of their results	39
4.3	Influence of the sampling window width	45
4.3.1	Influence of real data features	46
5	Analyzing real data and performing direction reconstruction	49
5.1	Creating ToT pulses from real IceCube data	49
5.1.1	Evaluating setups over the whole dynamic range	52
5.2	Performance testing: Direction reconstruction on ToT pulses	56
5.2.1	Direction reconstruction in IceCube	56
5.2.2	Determining the incident direction	58
5.2.3	Results and evaluation	62

Introduction

FOR thousands of years people observe the sky for scientific motivation, to navigate or even for religious reasons. The Nebra sky disk crafted around 1600 BC makes astronomy one of the oldest subjects in science. For most of the time, people were restricted to the optical frequencies of the electromagnetic spectrum discovering stars and galaxies. It was only during the past century when science offered new ways of observation developing new particle detectors and optical instruments exploring deeper into space than ever before.

One leading experiment for astroparticle physics is the IceCube detector located near the south pole built deep in the Antarctic glacier. It utilizes neutrinos as messengers from the high-energy universe and detects their interactions in the ice via Cherenkov light. To achieve that an array of thousands of optical sensors spans a cubic kilometer of instrumented volume.

With the experiment's construction completed in 2011 it provided renowned results like the detection of cosmological neutrinos. Yet, a further expansion is planned to increase the volume and thus the number of detections. This would, for example, advance significantly the search for point sources of neutrinos.

One promising candidate for a new optical module is the multi-PMT Digital Optical Module (mDOM). Its distinctive feature is to make use of several small photomultipliers instead of one increasing the sensitive area with 4π angular acceptance for directional information and the possibility to identify local coincidences inside of one module. Due to strict limits on the power budget of this setup a power-saving time-over-threshold readout will be implemented.

It is subject to this thesis to study the features of such a readout and to optimize it within the technical limits given. To that end, a simulation is used to sample and reconstruct waveforms.

The first part concentrates on single photoelectron pulses as they represent the majority of signals the mDOM produces. A method will be introduced to optimize threshold positions using generated waveforms as input.

In the second part real IceCube data is taken as input waveform and analyzed in order to evaluate the performance of different threshold setups covering the whole dynamic region. In a further step, the incident direction

of a neutrino event is determined using the reconstructed pulses obtained from sampling by the time-over-threshold algorithm.

1 The neutrino as a messenger from the high-energy universe

IN this chapter neutrinos are introduced and the importance of these “ghost-like” particles for astronomy is deduced. In spite of their huge abundance in the universe, it is extremely difficult to detect them due to their low cross section for interaction with matter. We will see where high-energy neutrinos can originate from and how they interact leaving us with several requirements for a suitable neutrino detector.

1.1 Neutrinos in the Standard Model of particle physics

Let us begin the introduction by classifying the neutrino into the Standard Model of particle physics [1]. This model is a theory developed over the course of the second half of the 20th century with its theoretically predicted particles gradually confirmed in experiments and vice versa. An overview of these particles is shown in figure 1.1. It includes three of the four known fundamental forces: electromagnetic, weak and strong force. Gravitational interactions are not covered.

For each of these forces there is a carrier, a gauge boson (spin 1), namely the photon for the electromagnetic, W and Z bosons for the weak, and the gluon for strong interactions. The Higgs boson is needed to give mass to the fermions and, in particular, to the W and Z boson. It is a scalar boson (spin 0) and was the final particle to be discovered in 2012 [2].

The ordinary matter we can experience consists of fermions (spin 1/2) which are divided into quarks and leptons. Both interact weakly while the quarks additionally interact strongly. Quarks build up mesons (quark - anti-quark) and baryons (3 quarks) which include protons (uud) and neutrons (udd), the “bricks” of nuclei. Together with the leptonic electron, they form atoms enabling chemistry and biology. It is in the leptons where we also find neutrinos. As with all fermions, there are three so-called generations and thus three different flavors of neutrinos: electron, muon and tau neutrino. The first neutrino to be postulated turned out to be the electron neutrino. In 1930 Pauli concluded that in order to explain the

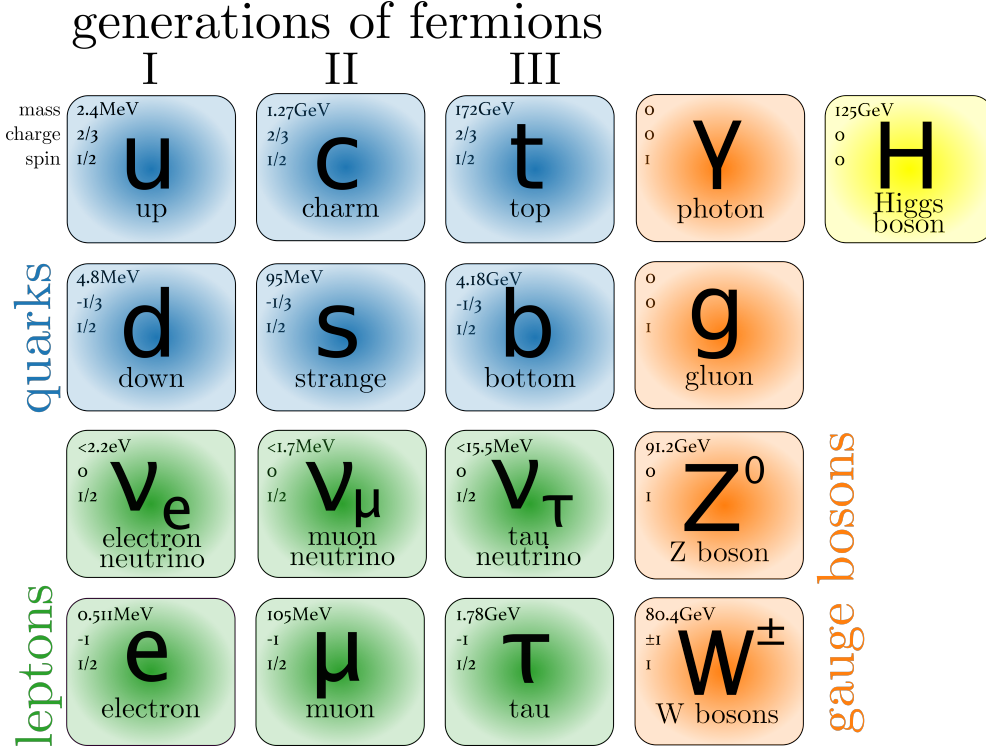


Figure 1.1: The Standard Model of particle physics. Quarks are displayed in blue, leptons in green. They are fermions and together form matter as we know it. The gauge bosons, which are the carriers of the fundamental forces, are shown in orange. Completing the model is the Higgs particle.

electron's continuous energy spectrum in the beta decay there must be a third particle involved [3]. It had to be (almost) massless and electrically neutral. Because of this properties, it was only 1956 when it was first detected by Reines and Cowan [4].

Initially, neutrinos in the Standard Model had no mass at all. However, we know from oscillations between flavors that they must be massive particles ([5, 6]). This was achieved by measuring the ratio between the flavors of solar and atmospheric neutrinos and comparing them to the expected ratio from the underlying processes. The difference found can only be explained by oscillation. Determining the actual absolute value of the mass is still subject of current research, for example in the KATRIN experiment [7].

As mentioned above, neutrinos are electrically neutral. With the listed characteristics we are left with essentially one way neutrinos can be created or interact: through the weak force.

1.2 Messengers from the high-energy universe

Initially, all observations in astronomy were done in the optical range of the electromagnetic spectrum. With advancing technology over the course of the last century, more parts of the spectrum became available such as microwave, infrared or gamma frequencies. Each adding important information to the understanding of our universe, such as the cosmic microwave background radiation [8] or gamma-ray bursts resulting from star explosions [9]. Nonetheless, there is a downside to using photons in astronomy: they may scatter or be absorbed in, for instance, interstellar dust possibly losing the information they carry about their source. In the atmosphere of the Earth they create showers and produce a signal that can be detected and reconstructed, successfully achieved by experiments like H.E.S.S. [10]. However, photons are not the only messengers from space we can utilize. Massive particles are also part of the cosmic radiation. They are mostly high-energetic protons or light nuclei originating from outside the Solar System [11]. But because they are charged particles they are deflected by magnetic fields on their way to Earth. Hence, their direction information is often lost completely.

Yet there is another particle which is suited very well for astronomical

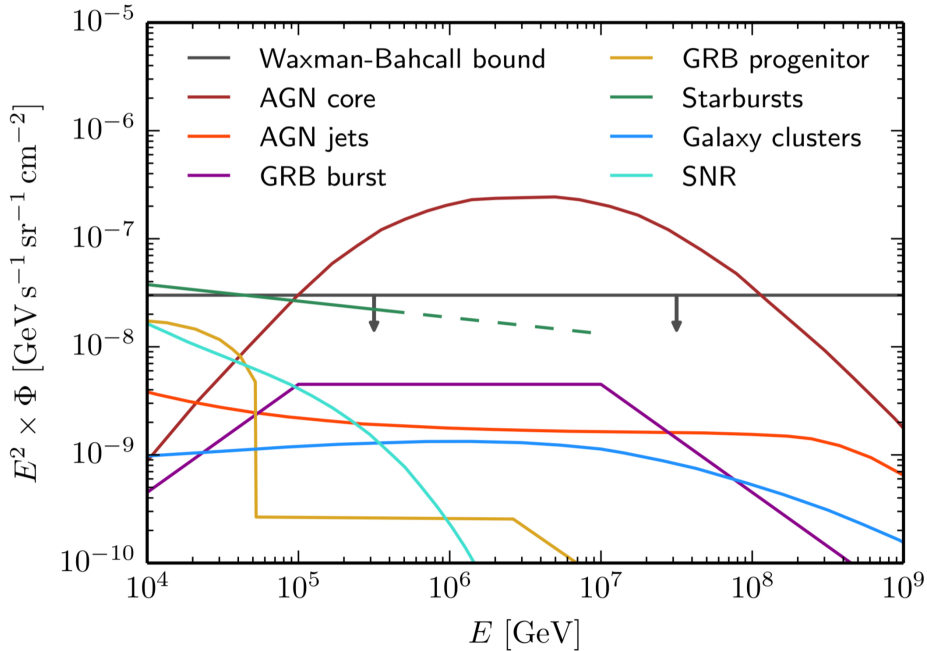


Figure 1.2: All flavor neutrino flux Φ scaled by E^2 versus their energy E . Note that these are theoretical predictions and that they can vary from author to author (taken from [12]).

observations: the neutrino. It only interacts weakly having a tiny cross section to do so. This is both a blessing and a curse at the same time. It guarantees us that the neutrino is not deflected or stopped by any matter on its way to Earth but simultaneously makes detection a difficult task. We will learn more about the detection principle in IceCube in chapter 2.

A further and relatively new form of astronomy shall get an honorable mention here: Detecting gravitational waves. This was managed by the LIGO and Virgo cooperation 2017 for the first time [13]. They measured a wave originating from the merging of a binary neutron star system.

Now that we have identified neutrinos as a reliable messenger for information from cosmological objects, let us see what characterizes their sources.

There are quite a few possible candidates for emitting high-energetic neutrinos of which [14] gives a good overview. The principle in each case is similar: cosmic acceleration sites produce hadrons that in turn decay and release neutrinos.

The preferred model for describing the acceleration process is the (first order) Fermi acceleration [15]. It predicts that when a shock wave propagates through a medium energy is transferred to charged particles. Here the shock wave can be understood as a magnetic mirror: if a particle happens to move towards the wavefront it is reflected without energy loss because of the magnetic inhomogeneities preceding and following the wave. If the particle originally has sufficient energy (i.e. is not slowed down by collisions) the energy transfer to it is very efficient and can happen multiple times. The term “first order” refers to the fact that the relative energy gain per scattering $\Delta E/E$ is directly proportional to the velocity of the shock wave v divided by the speed of light:

$$\frac{\Delta E}{E} \propto \frac{v}{c}. \quad (1.1)$$

Minor modifications to this formula give precise predictions of the energy spectrum of cosmic rays. The neutrinos, we were initially interested in, cannot be accelerated like described because they carry no electric charge. This means they have to come from particle decays.

With the energies involved, pions, the lightest mesons, are created in great quantities, for example when protons scatter off ambient photons (1.2) [16]. The pions then decay into muons and neutrinos and eventually into electrons and further neutrinos (1.3):

$$\begin{aligned} p + \gamma &\rightarrow p + \pi^0 \text{ or} \\ p + \gamma &\rightarrow \pi^+ + n \end{aligned} \quad (1.2)$$

$$\begin{aligned} \pi^+ &\rightarrow \mu^+ + \nu_\mu \rightarrow e^+ + \nu_e + \bar{\nu}_\mu + \nu_\mu \\ \pi^- &\rightarrow \mu^- + \bar{\nu}_\mu \rightarrow e^- + \bar{\nu}_e + \nu_\mu + \bar{\nu}_\mu \\ \pi^0 &\rightarrow 2\gamma. \end{aligned} \quad (1.3)$$

The decay of the π^0 into a photon indicates that neutrinos and gamma rays can coincide from cosmic acceleration sites. That leads us to the question of what the sources actually are. Here are the most probable candidates whose fluxes are shown in figure 1.2:

- In a Gamma Ray Burst (GRB) a huge output of gamma rays is measured lasting for milliseconds up to several minutes [17]. The first records of GRBs date back to the 1960s when a US military satellite was looking for nuclear weapon tests. Not until 6 years later the cause of the signal was identified as coming from space. The origin of GRBs is believed to be a core-collapse of a supermassive star or the merging of compact objects (neutron stars or black holes). The energy is emitted in two opposite directions creating so-called “jets”. Within these jets the acceleration due to the shock fronts takes place. If the jet points towards Earth it will be detectable as an emitter of high-energetic rays. So far no coincidence between gamma rays and neutrinos from a GRB has been found.
- Active Galactic Nuclei (AGN) are supermassive black holes in the center of a galaxy [18]. Black holes have the property of attracting all matter nearby because of their immense gravitational potential. This and conservation of angular momentum results in an accretion disc rotating around the black hole as matter falls into it. Perpendicular to the disc at the poles of the black hole jets of relativistic particles are observed. In figure 1.3 left such an AGN is illustrated. Again it is in the jets where the particles get accelerated and decay, producing neutrinos.
- The remnants of supernova explosions (SNR) are a good example for shock waves energizing the matter as they can be directly observed [19]. In picture 1.3, right, the shock front of “Tycho’s supernova”, a star explosion observed by Danish astronomer Tycho Brahe in 1572, is visible as the outer blue region. Their isotropic emission renders discovery of neutrinos from these sources challenging.
- Starburst galaxies are galaxies with a high rate of star formation and thus also host a large amount of supernovae [14]. Additionally, they contain plenty of gas with which accelerated rays can interact, yielding neutrinos.
- Finally, there are galaxy clusters, the largest structures in the known universe [14]. Shock fronts were detected with the Chandra X-ray Observatory originating from matter falling into knots of high density.

In figure 1.2 the Waxman-Bahcall bound is also included predicting a model-independent upper bound to the flux of high-energy neutrinos [20].

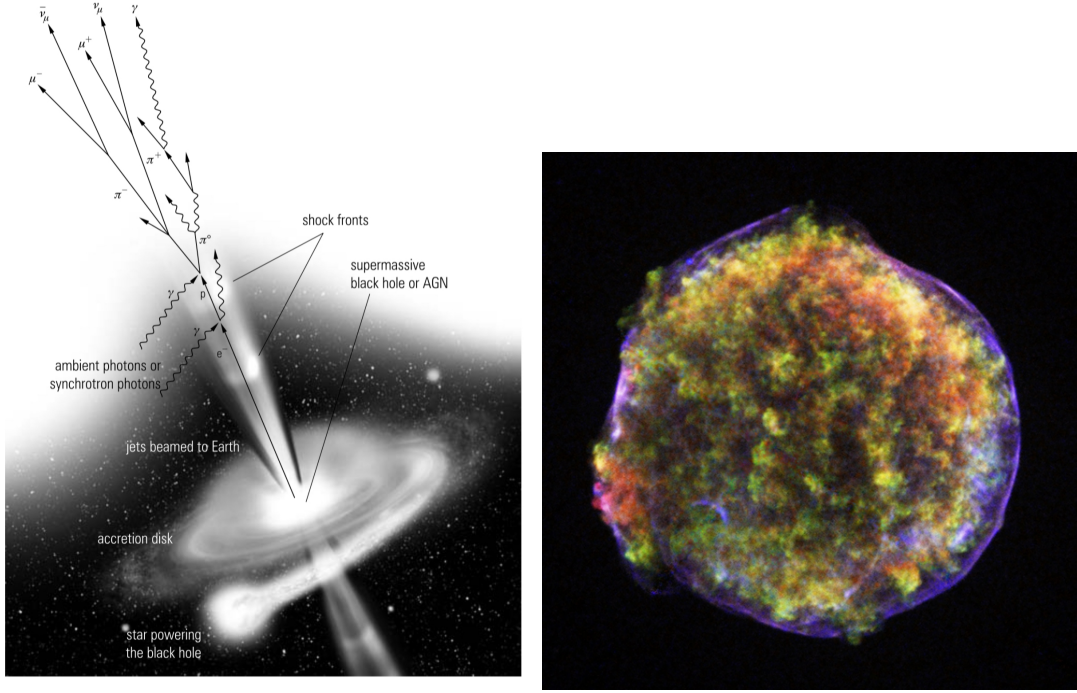


Figure 1.3: Left: Artistic representation of an active galactic center with its accretion disc and jets. It functions as a hadronic accelerator with particles decaying into neutrinos among other particles (taken from [16], p. 74). Right: X-ray image of Tycho's supernova by the NASA satellite Chandra. In blue the shock front is visible as it propagates (courtesy NASA/CXC/Rutgers/J.Warren & J.Hughes et al.).

It is restricted to neutrino production by accelerated particles as discussed above (e.g. AGN jets and GRBs).

One trait all sources have in common is a low flux of neutrinos that reach the Earth. Combined with a low cross section and the high energies we are interested in, a large active volume of the detector is needed to measure the rare occurrences of interactions. Also, we want to be able to detect the whole event which can, depending on the detection mechanism, span hundreds of meters.

1.3 Neutrino interactions

In order to understand how highly energetic neutrinos can be detected, we need to take a look at the interaction mechanism with special attention being paid to the expected outgoing particles.

Depending on their energy neutrinos can engage in different weak interactions. Starting at threshold with coherent scattering and capture in nuclei we have the inverse beta decay at neutrino energies of several MeV [21]. With energies in the low GeV range quasi-elastic scattering and

production of light particles such as pions and kaons via baryon resonances come into play. If we go one step further, neutrinos of 20 GeV and beyond are able to resolve the inner structure of nuclei. In a process called deep inelastic scattering they scatter off individual quarks instead of the whole composite. Since this is the energy region of interest let us get into detail here.

Figure 1.4 shows schematic Feynman diagrams of neutral current (a) and charged current (b-d) interactions of deep inelastic scattering of a neutrino and a nucleus. In the first case a Z^0 is exchanged between the

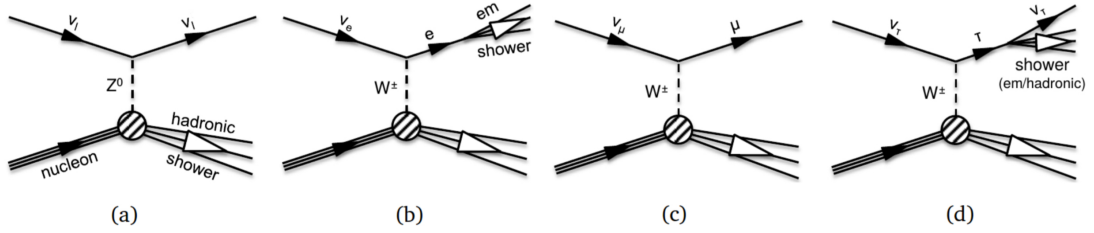


Figure 1.4: Deep inelastic scattering by a neutrino off a nucleus. a) shows the neutral current interaction creating a hadronic shower. b)-d) shows charged current interactions for each neutrino flavor and their resulting particles (taken from [22], modified).

neutrino and a quark of the nucleus. The resulting hadronic shower of the excited quark will be detectable. This interaction is possible for all three neutrino flavors.

In the charged current interactions, with the exchange of a W^\pm boson, the neutrino is converted into its corresponding leptonic partner. The hadronic shower is present again. Different flavors result in different signatures in a detector such as IceCube as follows:

- An electron neutrino interaction creates an electron which causes an electromagnetic cascade when depositing its energy. As in the case of a hadronic shower, the origin is basically point-like because of the high cross section of the particles for interaction with the surrounding medium. This means that the signature of such an event would look near-spherical (see figure 1.5, left). Note that it is not possible to distinguish between hadronic and electromagnetic showers.
- A muon neutrino interaction creates a muon which travels considerably farther through matter having a much larger mean free path. Thus a track is left in the detector (figure 1.5, middle).
- A tau neutrino interaction creates a tau that decays either into

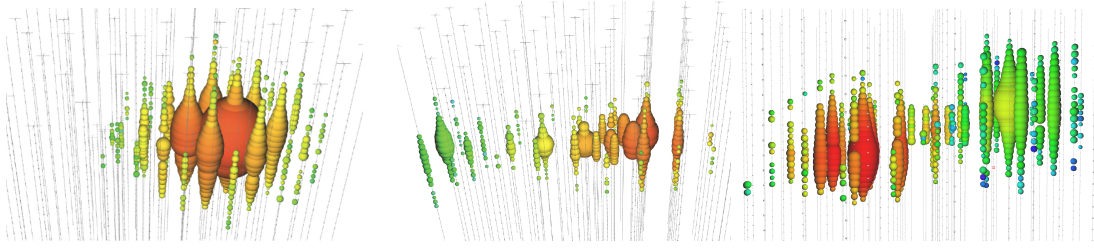



Figure 1.5: Left: Signature of an electron neutrino interaction causing a cascade shown in the IceCube event display. Red marks earlier detection, blue for later times. Middle: A track signature caused by a muon neutrino. Right: A double bang created by a tau neutrino where the tau decayed for example into an electron. (pictures courtesy of the IceCube Collaboration).

pions giving a hadronic shower or into an electron or a muon, each time accompanied by (anti-) neutrinos to ensure lepton number conservation. Two signals in different places, one hadronic from the neutrino interaction and one from the decay particle, are called a “double-bang” (figure 1.5, right).

Having learned about how different signatures arise depending on the incident particles, the question that arises is: How is it possible to make them visible in an experiment? This leads us to the next chapter where the detection principle will be explained together with the actual realization namely the IceCube detector.

2 Detecting neutrinos with IceCube and future extensions

 THE IceCube Neutrino Observatory is a km³ detector located near the Amundsen–Scott South Pole Station in Antarctica [23]. However, its extent is not directly apparent; it is arranged way below the surface, deep in the Antarctic glacier. In this chapter we will break down how it can be used to do neutrino astronomy, what it takes to record a signal and then report on the present results. It will also become clear why it is beneficial to extend the detector even further and what opportunities new optical modules have to offer.

2.1 The detection principle in large volume experiments

In the last chapter we left off with the creation of secondary particles in weak interactions by the neutrino in the ice. The fact that those neutrinos of interest feature energies up to several PeV means that also the secondary particles are relativistic. Whenever charged particles in a medium travel faster than the phase velocity of light in that medium, so-called Cherenkov radiation is emitted [24]. The distinct blue light is electric dipole radiation from the surrounding medium which is polarized by the passing particle. In the case of particles with slow velocity the medium's dipoles (for instance water molecules in ice) are able to arrange in time to balance out the charge allocation caused by the moving particle (see figure 2.1, left case). If, however, the particle moves faster than the exchange particles of the electromagnetic force, the photons, unmatched dipoles of the molecules create a resulting electromagnetic dipole \vec{I}_{tot} (figure 2.1, right case) which is the cause of the emission of radiation.

This Cherenkov light can be detected in experiments such as IceCube. Hence the active volume is equipped with thousands of light sensors, the so-called Digital Optical Modules (DOMs), detecting photons emitted by neutrino interactions and their secondary particles. We will first see a few facts and figures about the detector and then study how the DOM works.

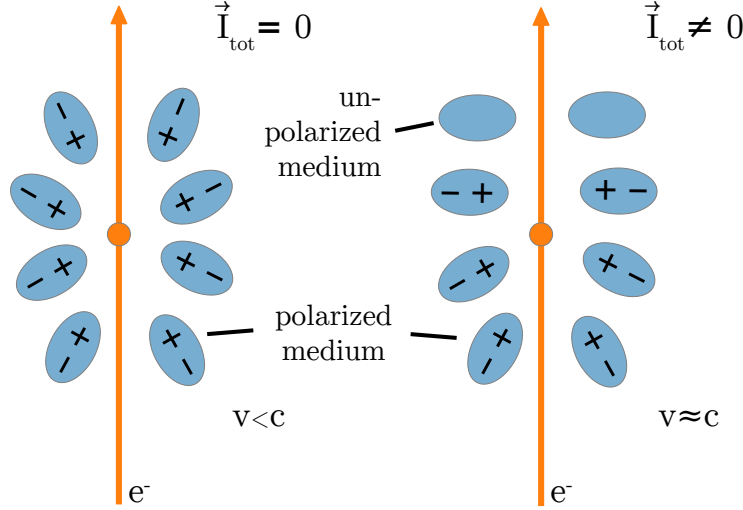


Figure 2.1: Left: A charged particle (an electron for example) moves relatively slowly through a polarizable medium and causes the dipoles to arrange themselves leaving no resulting overall dipole. Right: The particle moves relativistically and the medium's dipoles cannot balance the charge allocation resulting in a dipole \vec{I}_{tot} emitting Cherenkov radiation.

2.2 The IceCube detector and the Digital Optical Module

The IceCube detector is an array of 86 strings with 60 optical modules each [23]. A schematic overview is depicted in figure 2.2. Instrumentation reaches from 1.5 km beneath the surface to 2.5 km into the glacier. With its hexagonal grid and a horizontal distance of 125 m between the strings it covers an active volume of $\sim 1 \text{ km}^3$. The strings have a vertical spacing of 17 m and were lowered into boreholes drilled with hot water under high-pressure.

Data from each module is transferred via copper cables, that also provide power, to a central computing facility, the IceCube Laboratory. Being saved to hard drive there, the data is also sent by satellite to other IceCube facilities for further processing.

With its extent of one gigaton of Antarctic ice as detector material it is designed to look for neutrinos in the TeV range but additionally provides the opportunity to study neutrinos with energies as low as 10 GeV in the form of DeepCore; a subdetector with much denser instrumentation [25]. This allows for investigation of neutrino oscillations and for indirect search for dark matter.

A further feature is IceTop, an entirety of 81 tanks of ice with 4 DOMs each at the surface to detect cosmic rays and atmospheric showers [26]. Not only does it serve as a veto for atmospheric muons of the southern

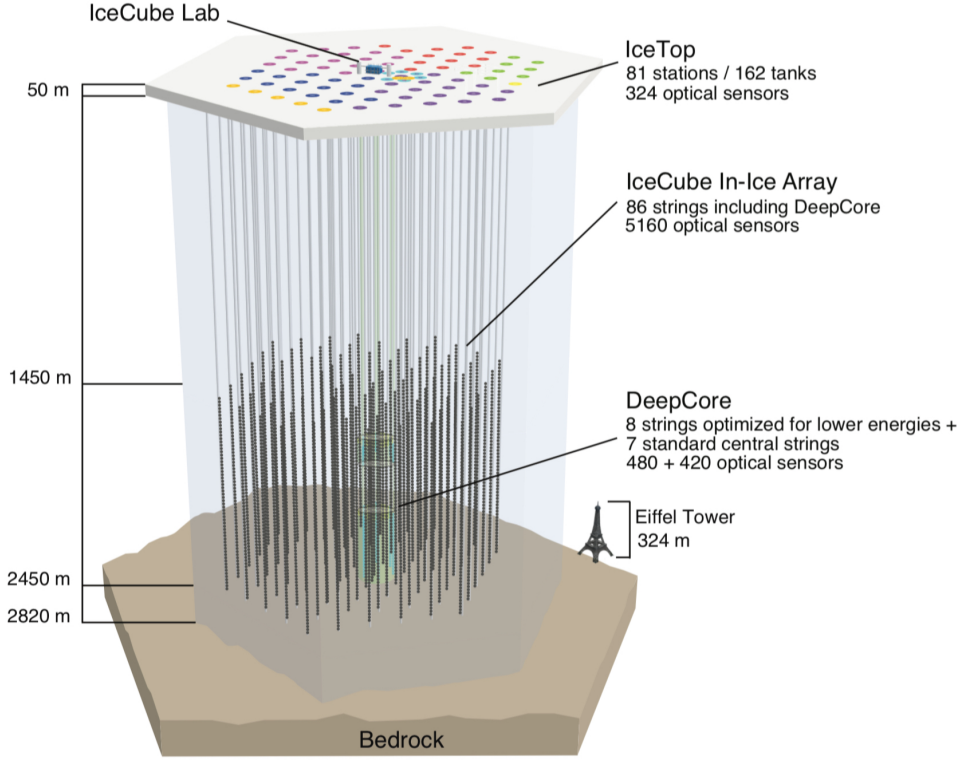


Figure 2.2: Illustration of the IceCube detector as built at the South Pole. The experiment consists of the service station IceCube Lab and the IceTop detector at the surface together with the in-ice strings about 1.5 km below surface including DeepCore equipped with a much denser instrumentation (picture courtesy of the IceCube collaboration).

hemisphere but it also offers the chance to conduct research, for example measuring the fraction of heavy cosmic rays (heavy nuclei) to light cosmic rays (e.g. protons) when combined with the underground detector.

Construction began in the austral summer of 2004 with the first string being deployed in January 2005 [23]. In January 2011 building was completed having installed 5160 DOMs in ice and additional 324 in IceTop's tanks.

A schematic view of the implemented Digital Optical Module can be seen in figure 2.3, left. The outer glass sphere holds up the pressure created by the surrounding ice, peaking while deployment when the borehole refreezes, and is 13 inch in diameter. Attached to the outside there are cables that provide data transfer and power supply simultaneously and a harness holding the DOM during deployment. The lower part houses a 10-inch photomultiplier tube (PMT) which is caged by a mu-metal grid for magnetic shielding. The PMT is the light detection device of the DOM. For both better optical coupling and mechanical support a gel is filled in between glass sphere and PMT. In the upper part, the base of the PMT and electronics are located. The Main Board is fit around the neck of the

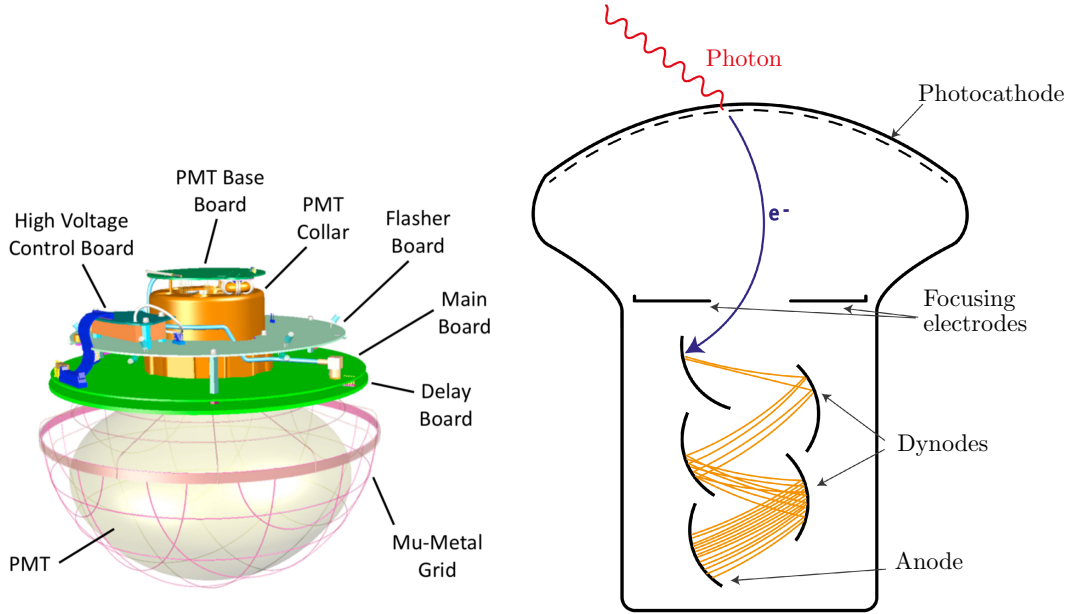


Figure 2.3: Left: Schematic view of the Digital Optical Module (picture courtesy of the IceCube collaboration). Right: Schematic drawing and working principle of a PMT. A photon hits the photocathode creating an electron which is then multiplied by the dynode system. At the anode the signal is read out (picture courtesy Martin Unland).

PMT containing data acquisition, control, calibration, communication, and low-voltage power conversion. Separate circuit boards are in place for the generation of high voltage for the PMT, for delaying PMT signals and for light flashers with which other DOMs can be calibrated (see 2.4).

Let us continue where we left off describing the detection principle. A Cherenkov photon was created and now we follow the path of the signal through the DOM.

First, the photon hits the photocathode of the PMT releasing an electron due to the photoelectric effect (see figure 2.3, right) [27]. The inner part of the PMT consists of a dynode structure where each dynode has a different potential applied by a high voltage power supply, including a potential difference between the first dynode and the photocathode. Because of the resulting electric field the electron is accelerated towards the first dynode with the focusing electrodes guiding the electron onto the dynode system. This single electron is then multiplied by passing through the dynodes in a statistical process. At each dynode an incident electron produces other electrons equivalent to its energy. Thus many electrons hit the anode where the signal is measured. This can either be the anode's voltage as a function of time or, equivalently, the accumulated charge. In IceCube the former is the case making this the analog signal of the PMT for the Main Board [23]. To get the total charge, the voltage signal has to be integrated over time and divided by the front end impedance. On

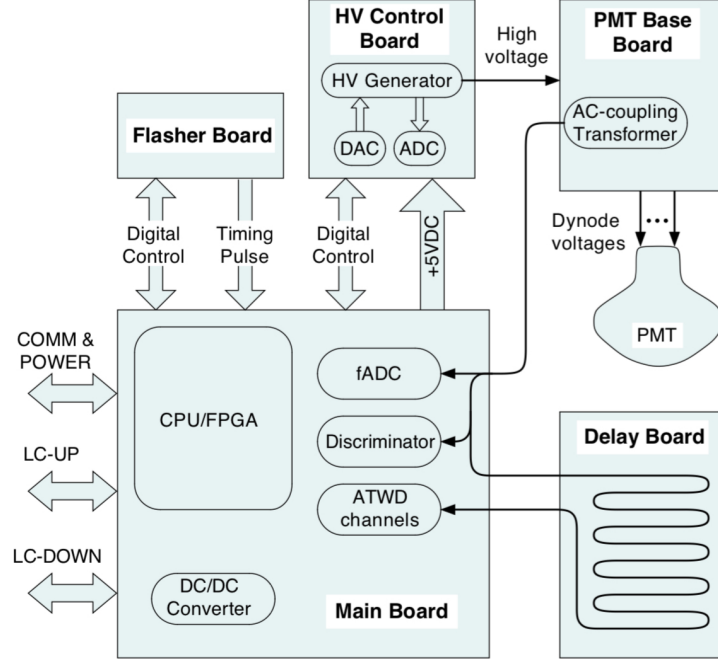


Figure 2.4: Simplified overview of the Main Board and the other boards used in data acquisition (taken from [23]).

average, a recorded charge of one photoelectron (pe) corresponds to one photon hitting the photocathode.

The subsequent data flow can be tracked in figure 2.5. First, the PMT waveforms are amplified and compared to a trigger threshold of 0.25 pe. If the signal surpasses the level a “launch” is reported initiating the digitizing process. Meanwhile the signal is stored in a delay of 10 m copper trace for 75 ns. Following that, 3 channels of an Analog Transient Waveform Digitizer (ATWD) with different amplifier gains for small signals (high gain) to signals close to saturation of the PMT (low gain) are ready to digitize the waveform with 300 Msps (3.33 ns time bin length). Starting at high gain the value is lowered if a certain threshold is surpassed and the gain is adjusted by choosing the next channel thus covering a wide dynamic range of the PMT. Each channel has a capacitor array length of 128 yielding an overall recording duration of 427 ns. However, this recording time only allows to detect photons produced tens of meters away from the DOM. Photons from farther away are recorded with a fast Analog Digital Converter (fADC) with 40 Msps recording for 6.4 μ s after the launch. A comparison of the waveforms from the described digitizers is shown in figure 2.6. The ATWD, on top, has a much finer binning and is able to resolve several photons of different arrival times while the fADC records for much longer.

After compression the signal is ready to be sent to the surface.

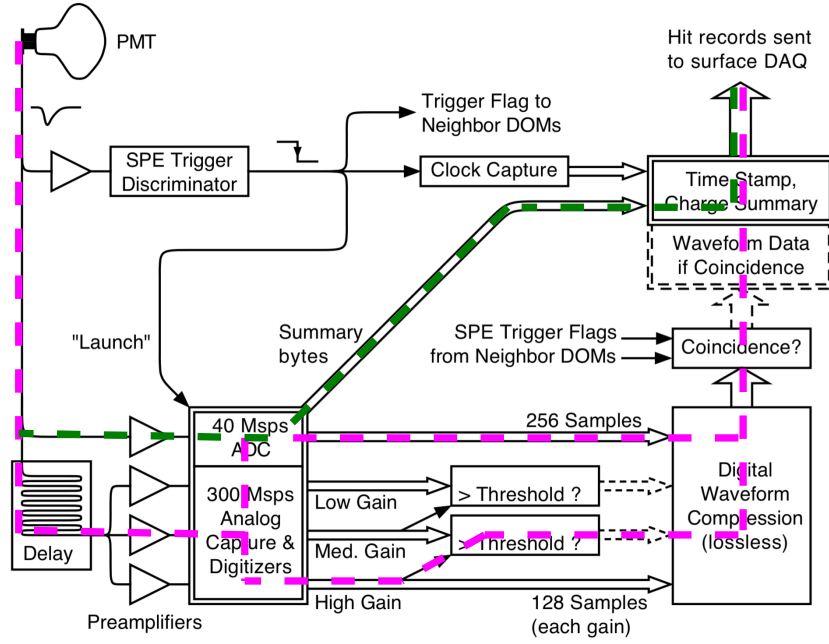


Figure 2.5: Circuitry to visualize the data acquisition from the PMT over digitization to transfer to the surface. In pink the flow of the full waveform information is drawn, whereas in green only a time-stamped total charge is reported (taken from [23]).

However, a check is performed whether there is a coincidence with a neighboring DOM (also recording a launch within $\pm 1 \mu\text{s}$). If this is not the case the process is canceled and only a time stamp and a charge summary are transmitted. Thereby, traffic from noise events is suppressed and the complete waveform data is only sent for coincident events. As it requires 50 ns to rearm the ATWD two chips are embedded to operate alternately to reduce deadtime.

2.3 First observations of astrophysical high-energy neutrinos

In the following section we will view some results published by the IceCube Collaboration so far. With at about 6 years of data 82 high-energy neutrinos were detected [28]. This sample is called “high-energy starting events (HESE)” specifying that only interactions are considered whose reconstructed vertex is located inside of the instrumented volume. Additionally, more than 6000 pe had to be detected which corresponds to a deposited energy of about 30 GeV.

Reconstruction of the event’s deposited energy allows plotting a spectrum of the neutrino flux. The result is shown in figure 2.7 as a

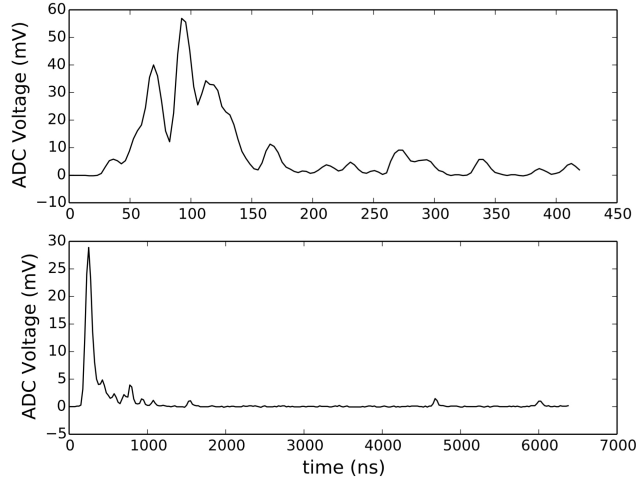


Figure 2.6: Comparison of waveforms as recorded by ATWD (top) and fADC (bottom) (taken from [23]).

rate of detection after 6 years versus the energy. Marked in red is the expected background from directly detecting atmospheric muons, created by air showers, that pass the veto. Blue are neutrinos originating from cosmic rays interacting in the atmosphere via decays of pions and kaons, with their combined uncertainty in grey. Another possible way to get atmospheric background neutrinos is considered in the pink line which predicts the flux from charm-containing mesons and their prompt decay. The measured data points in black lie predominately above the combined background curve meaning they are very likely extra-terrestrial. This gap increases with energy while it shows a good agreement with predictions at low energies (shaded area). The HESE make IceCube the first experiment to have detected neutrino energies of over one PeV.

Furthermore a direction reconstruction has been performed for this data set. The result is shown in figure 2.8. The purple color stands for a test statistic (TS) that corresponds to the likelihood of a point source being the origin of some of the neutrinos as opposed to an isotropic distribution. So far no significant clustering was found.

The three neutrino flavors causing their characteristic signatures have specific properties when it comes to reconstruction accuracy. For showers, created by electron neutrino interactions, the energy can be precisely determined as often the whole event is captured by the detector. However, direction reconstruction is more challenging yielding uncertainties of up to a few tens of degrees. Tracks, caused by muon neutrinos, on the contrary, are hardly ever fully contained in the detector which renders energy reconstruction difficult. Due to the nature of a "track," the direction can be determined to below one degree uncertainty. Double bangs have not been identified so far.

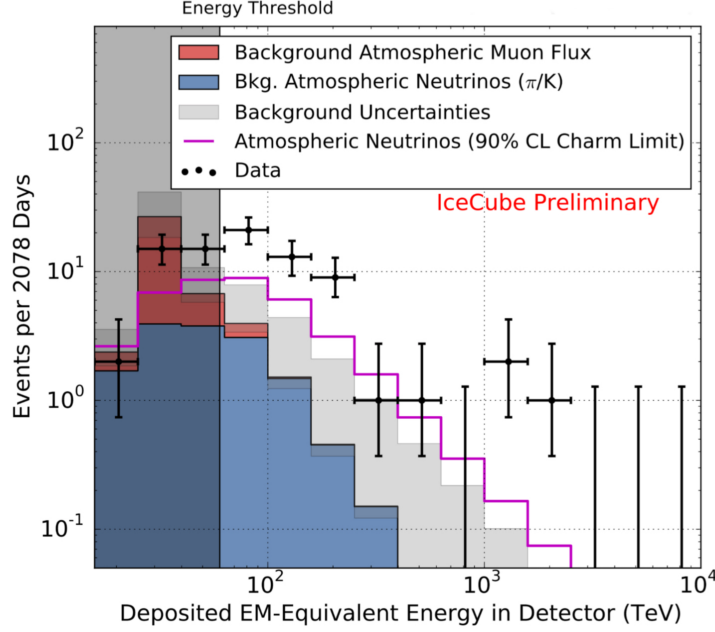


Figure 2.7: The detection rate of neutrinos after 6 years of data taking with the expected background from direct atmospheric muons and atmospheric neutrinos from mesonic decays. The data shows a significant flux of cosmic neutrinos (taken from [28]).

2.4 Future IceCube extensions and the mDOM

The low statistics thus far prevented IceCube from answering questions like that of the point sources, discussed before. A way to actively accelerate the rate of detection is to increase the size of the detector. This is the idea behind future IceCube extensions which are planned to be built around the existing detector array, for example, as drawn figure 2.9 [30]. Looking for neutrino energies in the PeV range it has an even sparser instrumentation spacing resulting in an overall active volume of up to 10 km^3 . At the other end of the energy range of the current IceCube detector, an even denser extension is planned for DeepCore, called PINGU, which is sensitive to neutrino energies of several GeV suited, for example, to study the neutrino mass hierarchy [31]. Also included in the “next-generation” design is an extended surface air shower array for atmospheric shower studies.

Deployment of added strings also provides the chance to develop new, more technologically advanced optical sensors. No less than several thousands of them will need to be installed. One promising candidate is the multi-PMT Digital Optical Module (mDOM) at which we will have a closer look (see [22] for detailed information).

As the name suggests, one important difference between the IceCube

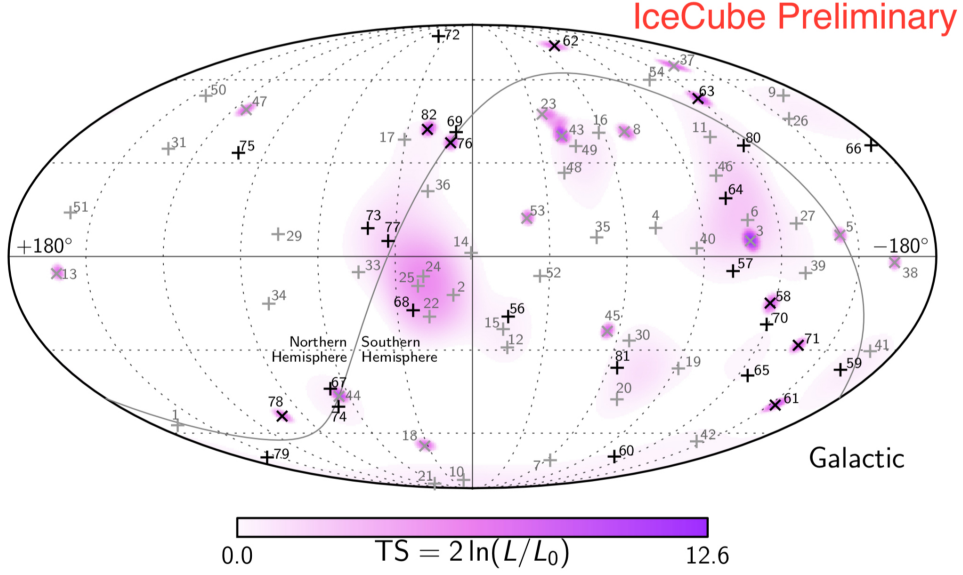


Figure 2.8: Directional distribution of HESE in a sky map. Cascades are marked with a + and tracks with a \times . The black colored events are the most recently observed. No significant clustering indicating a point-source has been observed (taken from [28]).

DOM and the mDOM is the instrumentation with photomultipliers. The new model features 24 3-inch PMTs facing all directions instead of one 10-inch “looking” downwards. The idea is adapted from the KM3NeT experiment, another large volume detector looking for neutrinos currently under construction in the Mediterranean Sea [32]. This design inherently has several advantages over the original module:

- A larger photocathode area: Adding up the sensitive area from all 24 PMTs an increase of a factor of > 2 compared to the DOM is achieved.
- 4π angular acceptance: Having PMTs facing all directions results in a near homogeneous coverage. See figure 2.11, right for a comparison between the P-DOM, an advanced version of the DOM, and the mDOM.
- Directional sensitivity: An array of PMTs allows for better directional reconstruction due to the possibility of identifying an incident direction of the photons with one single module.
- Enhanced photon counting: The mDOM will be able to distinguish between several single photons in different PMTs instead of producing a multi-photon signal like it would be detected by the DOM. This also allows for recording of local coincidences within one module enabling superior search for supernovae, for example, as well as rejecting correlated background.

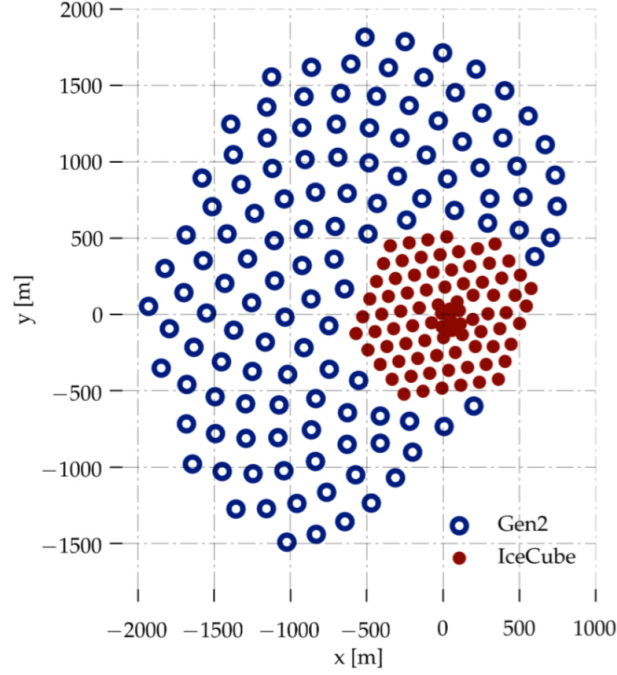


Figure 2.9: A possible footprint of a future extension adding strings around the old detector array (taken from [29]).

- Extension of the dynamic range: Photon hits are most probably split to multiple PMTs increasing the saturation limit of the whole module, assuming comparable dynamic ranges for small and large PMTs.

The mDOM's hardware design is displayed in figure 2.11 left: Like in the case of the IceCube DOM a pressure vessel is needed which is, with 14 inches in diameter, at about the same size as the original module so that the existing drilling equipment can be reused, saving costs. Inside, the PMTs are mounted onto a holding structure which includes reflectors to guide more photons towards the PMT's photocathodes, further increasing the effective area. Moreover, an optical gel will be used to reduce the difference in refractive indices, thus reducing reflection of photons.

In the equatorial plane, the main board can be found. Here, in the center of the module, the electronics are located. Each PMT's base generates its own high voltage via a Cockcroft Walton circuit from a low voltage input in order to reduce the overall power consumption. This principle is already successfully implemented in the KM3NeT module [33]. Adding to the power consumption, each PMT is read out separately to realize the full potential of a multi-PMT advance.

Depending on the actual final design for a next-generation detector at about 3 W will be available for a single module. For the readout, a PMT is left with a budget of only ~ 60 mW. To satisfy that requirement the approach is to use a power-saving time-over-threshold (ToT) readout to digitize the analog PMT signal right on the base. In this setup, only the

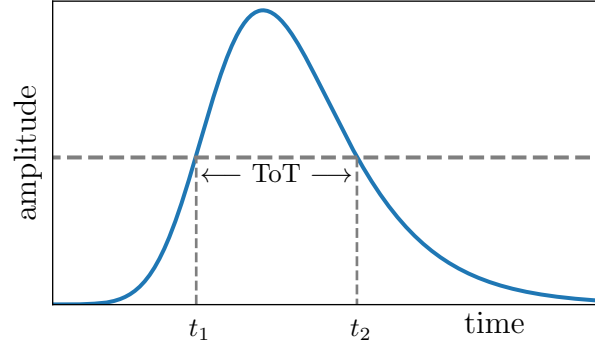


Figure 2.10: An analog amplitude signal (blue) is evaluated using one threshold. t_1 and t_2 denote the times of the leading and the trailing edge crossing the threshold. The ToT is then $t_2 - t_1$.

times of the leading and the trailing edge of the signal crossing an amplitude threshold are recorded (compare [34]). The number of photoelectrons is then proportional to the time the signal spent above the threshold. This principle is displayed in figure 2.10.

There are two different realizations currently under development [22]:

- A baseline concept where the waveform is passed to four discriminators with adjustable thresholds. A FPGA (Field Programmable Gate Array) on the main board determines the times of the leading and trailing edges, calculates the time over threshold and time-stamps the value. In order to speed up the process and for simplicity the circuitry is constructed from discrete parts. Currently, this is considered more as a fall-back solution.
- A more ambitious concept is using, by contrast, a custom-made ASIC (Application-Specific Integrated Circuit) on the base with 63 comparators, freely adjustable. Again a FPGA time-stamps the output of the ToT, which is also encoded to reduce the amount of data.

It is obvious that there is less information contained in a ToT signal than in a fully sampled waveform. It is subject to this work to simulate such a readout and test its performance with the aim of optimization.

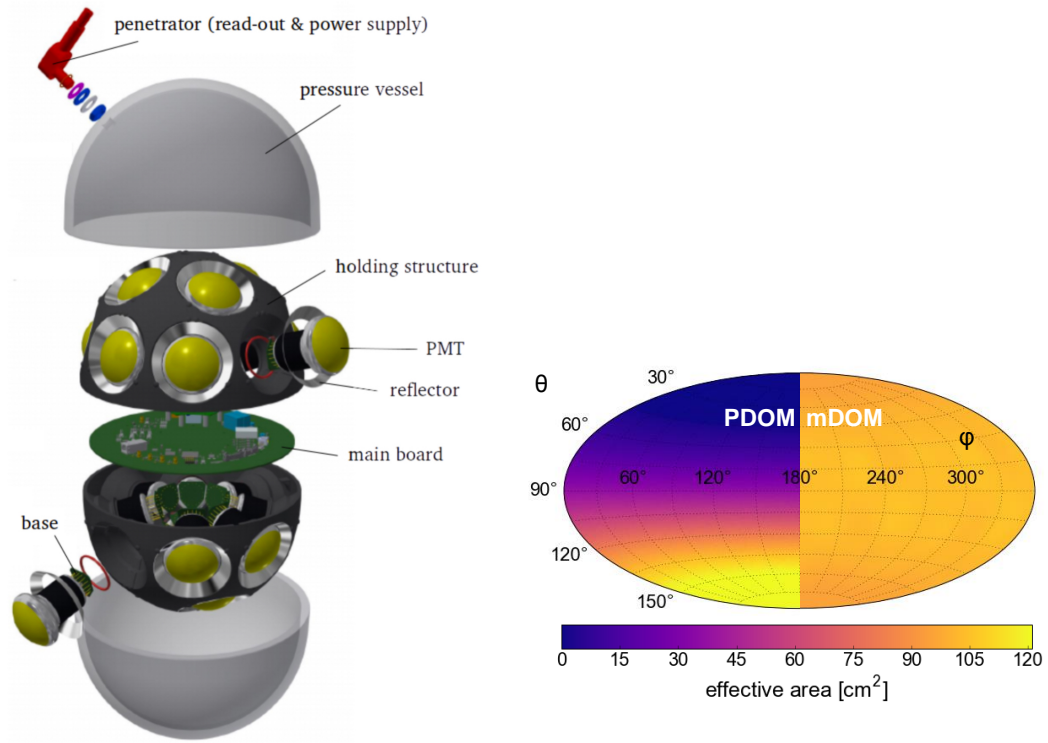



Figure 2.11: Left: Exploded view of the multi-PMT Digital Optical Module. 24 3-inch PMTs are mounted onto a holding structure separated by the electronics in the middle (picture courtesy of the Münster IceCube group). Right: Comparison of the effective areas between P-DOM and mDOM. The integrated effective area is larger in the case of the mDOM and it is sensitive to all directions homogeneously (taken from [22], modified).

3 Pulse reconstruction and simulation software

 THIS chapter presents an overview of the software framework used in this thesis and its operation principle.

Therefore, we continue with the signal obtained from the DOM and first examine how the incident photons are reconstructed in IceCube using deconvolution by a non-negative least squares (NNLS) method. Beforehand, the framework used for this, IceTray, will be introduced.

Next, a standalone simulation is presented in which a generated analog input is digitized using a time-over-threshold algorithm. Here, the same key features as in the original IceCube approach are used. The results of chapter 4 are based on this program.

Finally, the ToT algorithm will be used to analyze real IceCube data within the IceTray framework, taking waveforms as input and testing the quality of the reconstruction obtained with ToT. This provides the basis for the work in chapter 5.

3.1 The IceTray framework and pulse reconstruction in IceCube

IceTray is a multifunctional software package developed by the IceCube collaboration [35]. It supplies the framework to simulate and analyze events in the detector and, among many other features, provides a visualization tool we already encountered in figure 1.5. The name originates from the fact that the main process is a *tray* which consists of multiple *modules*. From now on, IceTray specific words are written in italics. An input file is passed on along the *tray* from one *module* to the next. The file format is called *I3File* which is a dynamic object every *module* can use or modify (e.g., add, delete, overwrite information). *I3Files* are structured into *frames*, namely the *I3Geometry* (*G-frame*), containing information about the location of the DOMs inside the detector, the *I3Calibration* (*C-frame*), where the calibration data for each optical module is stored, the *I3Detectorstatus* (*D-frame*), with detailed information about the characteristics of the single modules, the *I3DataAcquisition* (*Q-frame*), where recorded DOM hits and

waveforms are written to, and the *I3Physics* (*P-frame*), containing results of offline analysis.

As an example, it is instructive to look at a *tray* that reconstructs pulses out of raw data, since we will encounter that later. Figure 3.1

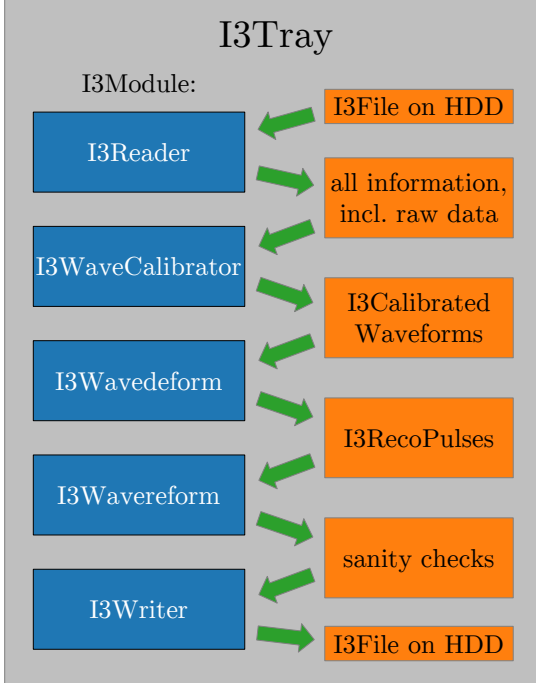


Figure 3.1: Work flow of an *I3Tray*. A data file is read and processed through several *modules* that add information. Shown is the case of *I3Wavedeform*, a module deconvolving the recorded DOM response to incident photons. Afterwards, the output can be written to the hard drive.

shows a schematic overview. At the beginning of each *tray* is the *I3Reader*, which renders the information contained in *I3Files* available for all following *modules*. The first action to be performed is *I3WaveCalibrator* which uses the raw data from the digitizers in the *Q-frame* and calibration data (*C-frame*) to create calibrated waveforms. Next, the *I3Wavedeform* performs the deconvolution of underlying (multi-) photon pulses from the calibrated waveforms using a single photoelectron template. This step will be explained in more detail in the next section. The output from this module are *I3RecoPulses*, the main result from this *tray*. *I3Wavereform* performs checks by comparing the input, the calibrated waveforms, with the reconstructed waveforms which are created by again convolving the *I3RecoPulses* with the pulse template. A χ^2 -like quantity produces a warning if a

certain value is exceeded, identifying, for example, failures in calibration. Lastly, the *I3File* is saved to hard drive by the *I3Writer*.

3.1.1 Deconvolution of the DOM response to photons

The *I3Wavedeform* uses a non-negative linear least squares (NNLS) algorithm [36] to deterministically deconvolve the single photoelectron response function from the waveforms recorded by the DOM's fADC and ATWD digitizers [37]. The working principle is the following:

- Load the waveform data into a vector. This data consists of the amplitudes and the respective time bin length. Both ATWD and

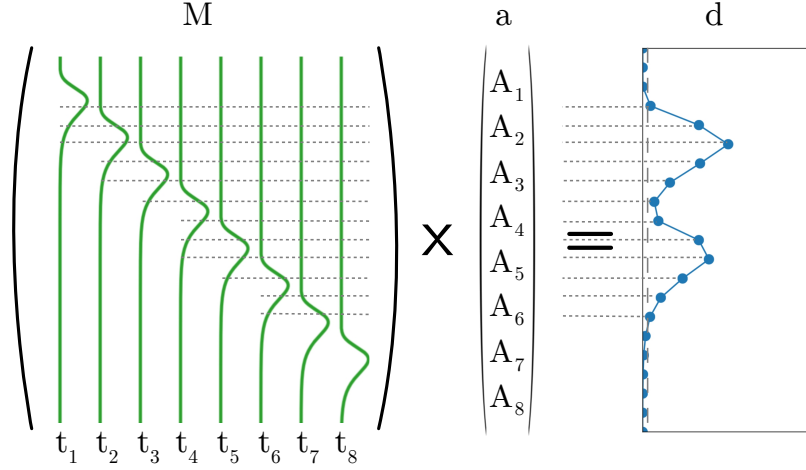


Figure 3.2: Representation of the linear equation $Ma = d$ to be solved: M contains single photoelectron pulse templates for all possible times. They are scaled by their corresponding amplitude A_i to best fit the data d . This method is called a non-negative least square fit. Afterwards, the vector a consists of the deconvolved pulse amplitudes and the t_i are their time stamps.

fADC are used while the latter is weighted less when the former is active. Considering information from both digitizers simultaneously prevents edge effects at the boundary of the ATWD.

- Set bins that are under the predetermined noise threshold to zero and reduce their weight.
- Create a set of possible pulses from a template. A number of pulses per bin can be set (e.g., 3 means a temporal spacing for the ATWD of 1.11 ns as it has a bin width of 3.33 ns). More pulses per bin improve the fit result but increase computing time immensely.
- Build a response matrix M out of the set of pulses that satisfies $Ma = d$ where a is a vector of amplitudes corresponding to each pulse and d the data to be fitted. An illustration of this process is shown in figure 3.2.
- Solve the equation for a by matrix inversion, yielding the pulse amplitudes A_i .

The result is a deconvolved series of incident photons detected with the DOM. The two values that fully characterize each pulse are its amplitude, A_i , and its time, t_i . This information is saved in the *I3RecoPulse* along with a note concerning which digitizers were used to record the signal. Most of the subsequent analysis is done directly using pulses underlining the importance of this *module* inside the IceTray package.

3.2 Standalone python simulation program

The standalone program used to simulate a time-over-threshold readout and the subsequent pulse reconstruction follows the same principle as discussed before. It generates “analog” waveforms as input, digitizes them using a particular algorithm and creates the data points to fit underlying pulses yielding the amplitudes and times.

For the purpose of optimization studies, a “*IceWavereform*” is also incorporated which builds a complete waveform again providing the opportunity to compare it to the input waveform.

The body of the code was already available in the Münster IceCube group. Several modifications have been made for this work, especially in

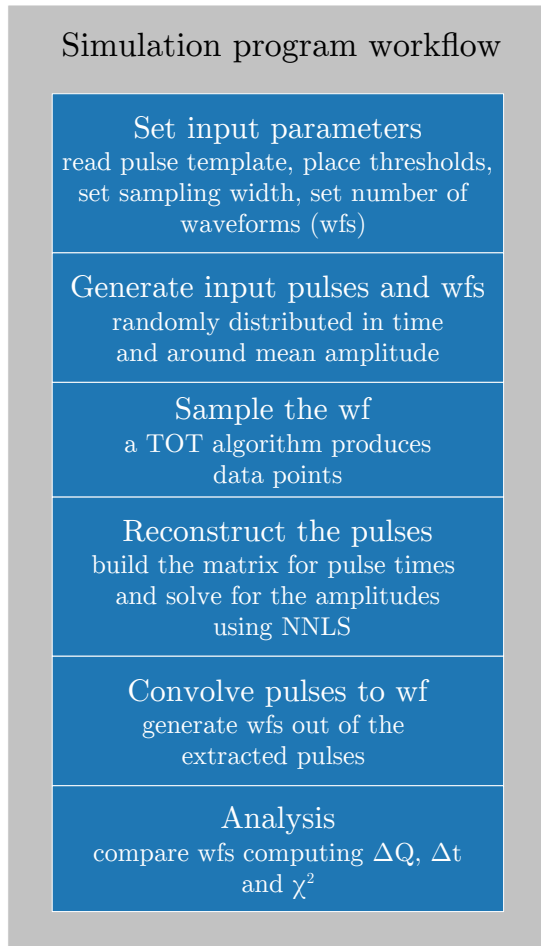


Figure 3.3: Workflow of the python standalone simulation program.

conjunction with the integration as a module in IceTray (see chapter 3.3 for detailed information). The program features several input parameters which can be varied in order to test their influence (see figure 3.3). There are the number of the thresholds and their placement, the sampling window’s width and the number of iterations; the number of waveforms being processed. Also at the beginning the single photoelectron (spe) pulse template is loaded. It is taken from the IceCube DOM as a generic PMT signal template.

Next, the “analog” waveform is generated out of pulses of randomly distributed amplitudes as well as random times which are convolved with the template. The sampling of the waveform by the ToT algorithm is subject to the next subsection. The output is a set of data points to which pulses are fitted using NNLS as described in chapter 3.1.1. However, there are small differences:

Here, a noise threshold does not need to be set specifically as it is simply the lowest threshold. Also, the number of pulses per bin is fixed at a value of 4 per 3 ns by the NNLS algorithm used.

In order to evaluate the quality of the result, the reconstructed

waveforms are formed and the difference in total charge and time are calculated as well as a χ^2 -like quantity comparing the two waveforms directly to each other.

3.2.1 The time-over-threshold algorithm

Now that we have an idea of what the ToT algorithm is going to produce, let us study it in detail. Figure 3.4 illustrates how the sampling is done. In the top part the original waveform is drawn in blue. Whenever its amplitude crosses one of the thresholds, the grey dashed horizontal lines, a data point is taken. These are represented as orange filled circles. The timing of these points is only known to a sample window width, drawn as dotted vertical lines. As a best guess of the time of crossing, the point is set into the center of the the time window. Typical values for the anticipated hardware are sampling widths of 1 – 3 ns corresponding to a sampling rate of 1 GHz to 333 MHz while a spe signal lasts for about 35 ns. To be able to successfully run the NNLS, additional input of data points is needed. Therefore, whenever thresholds are not crossed during a time window a point with less weight for the fit is created. They can be divided into three qualitatively different groups:

- The same threshold is cut again by the original amplitude, (1) in figure 3.4. That means the signal was either below or above the threshold without intersecting with any other. Thus, the sample points are set halfway in between as a best guess. Whether this is above or below the threshold is estimated by the slope computed from earlier information. In the depicted case the slope is positive between the first and the second threshold so the points are believed to be above the second threshold.
- A different threshold is cut as the next sample point with full weight is taken, (2) in figure 3.4. This means the curve must have risen or fallen between the two thresholds. No matter what the exact behavior was, the additional points are set in a straight line from the first orange point to the next.
- At the beginning and at the end, the data points are set to zero, (3) in figure 3.4. The lowest threshold (at for example 0.25 pe) corresponds to the noise threshold in the current IceCube *I3Wavedeform*. Hence this feature is inherently part of a ToT readout.

The orange dashed lines in the figure represent the results of the NNLS; the scaled pulses as found by the fit algorithm. However, this example illustrates that this should not be regarded as a physically relevant series of

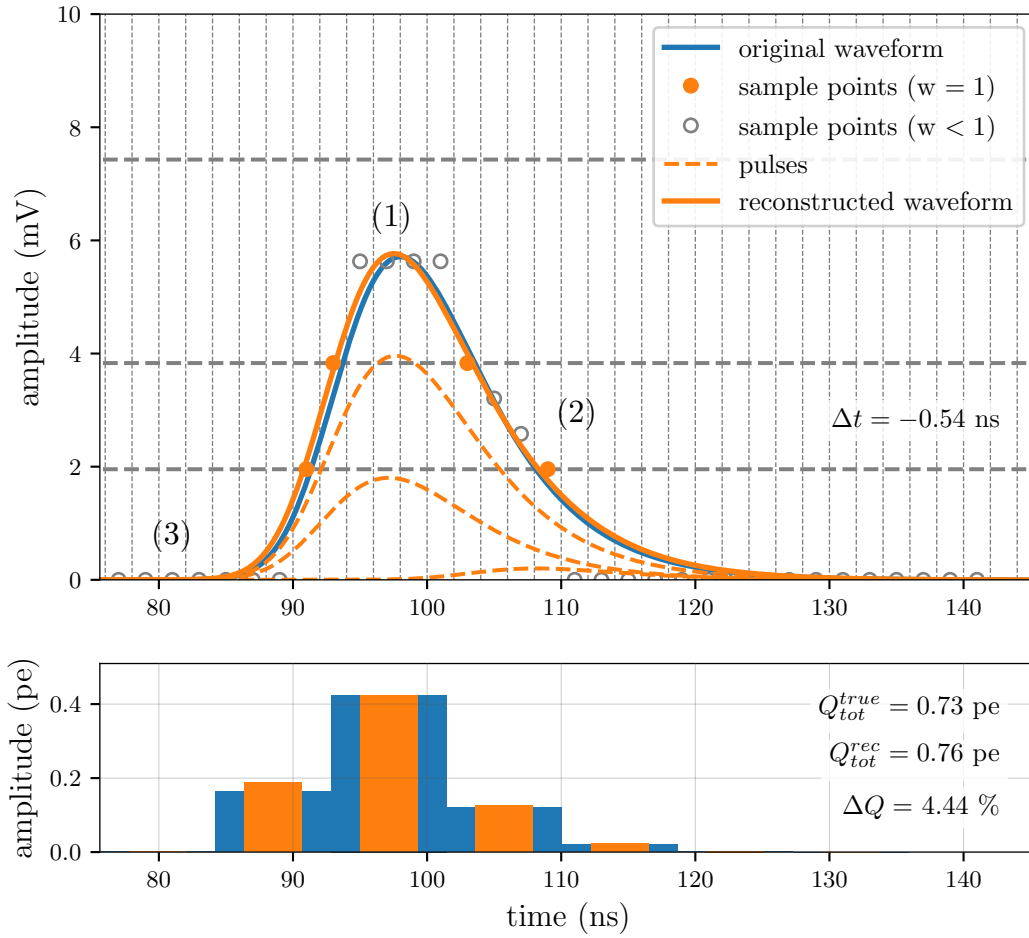


Figure 3.4: Top: Original and reconstructed waveform together with the different classes of sample points as created by the ToT algorithm. Vertical lines represent the sampling windows and the horizontal lines are three thresholds set. Bottom: Histogram of the total charge contained in the signal.

pulses but rather the sum of them can. That is the reconstructed waveform in orange, convolved like in *I3Wavereform*.

When we now try to evaluate the quality of the reconstruction there are two different approaches possible.

A physics motivated analysis looking at how well the total charge and the starting time of the waveform are reconstructed. In the first case, one can either sum up the amplitudes of all pulses or, equivalently, integrate over the area under the waveform. This is shown in the histogram at the bottom of figure 3.4. The quantity ΔQ is then given by the difference between the true value and the reconstructed value normalized to the true one in percent,

$$\Delta Q \equiv \frac{Q_{tot}^{rec} - Q_{tot}^{true}}{Q_{tot}^{true}} \cdot 100. \quad (3.1)$$

In order to compare the times a t_0 is defined as the point where a straight line going through 90 % and 10 % of the maximum amplitude crosses the abscissas (compare figure 3.5). The quantity Δt is then simply

$$\Delta t \equiv t_0^{rec} - t_0^{true}. \quad (3.2)$$

The other approach is to look solely mathematically at the equality of the two graphs. The quantity χ^2 is the relative difference per data point:

$$\chi^2 \equiv \frac{1}{N} \sum_{i=0}^N \frac{(a_i^{rec} - a_i^{true})^2}{a_i^{true}}. \quad (3.3)$$

It is derived from the general reduced χ^2 method. Here, N is the number of data points and a_i the amplitude of each point.

3.3 Incorporating the ToT algorithm into IceTray to analyze real data

The functionality of the standalone program has been extended by compiling it into an *I3Module* accepting waveforms as input and returning reconstructed pulses as output. For this, *I3WaveCalibrator* is run first, like in the example tray of figure 3.1. So, instead of randomly generated waveforms, data from the HESE event sample is used. Taking already calibrated waveforms implies of course that the input is only a pseudo-analog signal as it is already digitized. But due to the fine binning of the ATWD, a lot of original noise effects are still present testing the operability of the ToT digitization. Furthermore, the HESE data has been studied in great depth making it a perfect test sample as many analysis methods

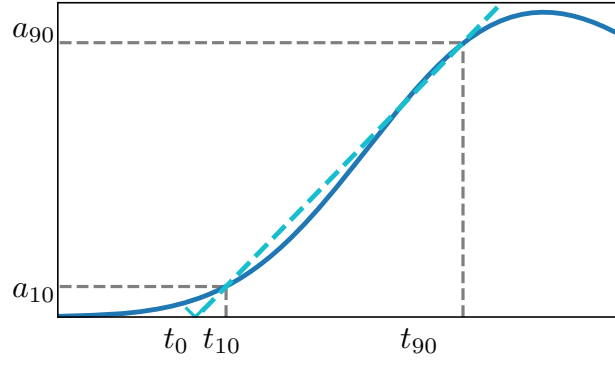


Figure 3.5: Definition of t_0 as the time assigned to the pulse. A line is fit through 90 % and 10 % of the maximum amplitude and crosses the x-axis at t_0 .

already exist. In the following, the modifications to the code and differences compared to generated input are listed.

One difference is that the bin width of the ATWD is 3.33 ns as opposed to the freely adjustable bin width in generated data. This results in the same bin width for the reconstructed waveform to ensure the two can be compared properly and additionally in the same sampling width used as it is not reasonable to choose a finer binning. The section 4.3.1 at the end of chapter 4 deals with this topic and serves as a transition to chapter 5.

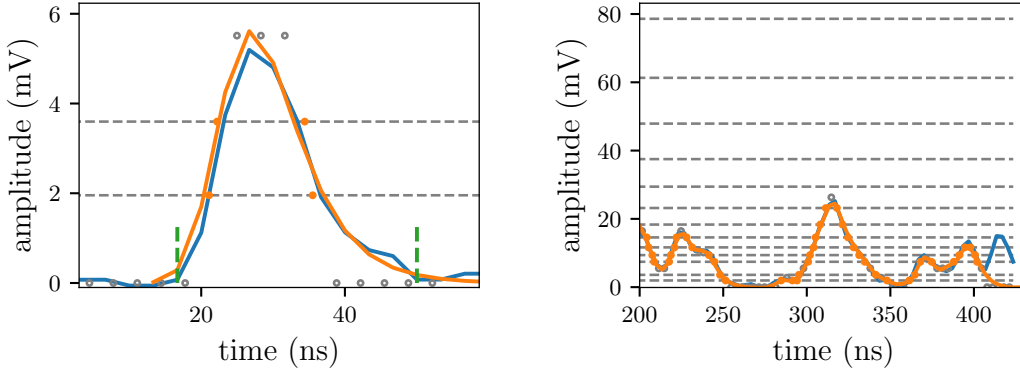


Figure 3.6: Left: A spe sampled by the ToT algorithm. The waveform is extended by points of amplitude zero before and after the pulse even though the original waveform fluctuates around the baseline. Note the rough binning of 3.33 ns. The green markers indicates the region of interest for comparison. Right: The end of the ATWD time window is treated specially: if the amplitude is still considerably high the last pulse is neglected for better comparability.

Often times the DOM signal consists of one photoelectron only

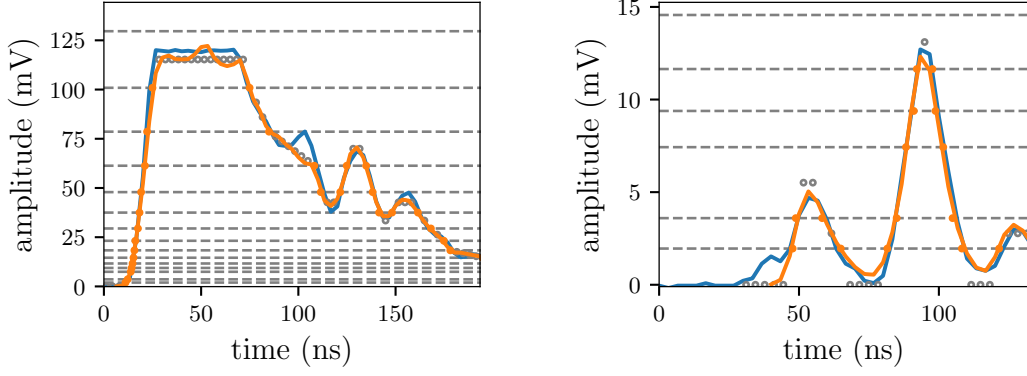


Figure 3.7: Left: Waveform of a saturated DOM. The actual charge of the first peak is challenging to evaluate, leaving saturated DOMs excluded from some studies. Right: Example of a special case where a small signal or a noise effect caused an overestimated Δt . t_0^{true} is calculated at the first pulse while t_0^{rec} is calculated at the second pulse (the first one that is sampled).

accompanied by a long baseline signal. For reasons of efficiency, the waveform is cropped five sampling windows after the lowest threshold was crossed for the last time and no more zero values are recorded as sample points (see figure 3.6, left). This saves time as fewer pulses have to be processed while still ensuring the NNLS fit results are satisfying.

A similar tweak is applied when comparing the waveforms to each other and calculating the ΔQ and the χ^2 : The regions of only noise (for example between two separated spe pulses) are neglected as they give a significant contribution to the χ^2 value when the original signal fluctuates around zero while the reconstructed waveform is smooth at zero. Thus both waveforms are cut after the reconstructed one falls below an amplitude of 0.05 mV. Figure 3.6, left, has the beginning and the end of the region in interest marked in green.

In this work, only the ATWD's waveform has been considered as the testbed it provides is sufficient in the aspired scope. However, that results in waveforms potentially being cut off at the end of the digitizer's recording window. To avoid that, the last peak is being neglected whenever the amplitude of the last data point is above a certain threshold. That also implies that no information from the fADC is available while the ATWD is active as it is a more sophisticated detail of the *I3Wavedeform*.

In very high-energetic events, such as the HESE, it often happens that one or more optical modules near the interaction point detect enough photons in a few nanoseconds to saturate the DOM. Such a signal can be seen in figure 3.7, left. These are challenging to analyze correctly with the ToT algorithm. That is why two different sets of analyzed data are created. One excluding all saturated DOMs when the actual quality parameters ΔQ , Δt and χ^2 are evaluated (chapter 5.1) and one including saturated

DOMs used for the direction reconstruction as these are most important here (chapter 5.2).

In a few incidents, the calculation of t_0^{true} had to be adjusted. In case there is a small non-zero signal before the first reconstructed pulse the algorithm would calculate the t_0^{true} using this first pulse but the t_0^{rec} using the second pulse leading to an overestimation of Δt . One such case is shown in figure 3.7, right. This will not be present in an actual setup as no features below the lowest threshold will be resolved. For this study, the workaround is to use a fixed, averaged slope for the line going through (t_{90}, a_{90}) depending on the signal's amplitude and calculating the t_0 out of that instead.

Lastly, mainly for clarity reasons, pulses coming from the NNLS are merged whenever they are less than 3 ns apart. As mentioned above, this does not change anything for the physics involved but only means that there are fewer pulses to work with for building the waveform and further analysis.

4 Optimizing threshold setups for single photoelectron pulses

ONE of the advantages of the multi-PMT approach the mDOM uses is the superior photon counting, including full digitization of single photoelectron waveforms. Because of the fact that several simultaneously arriving photons will most probably hit different PMTs, the great majority of signals will consist of spe pulses compared to rarely occurring high-energy events. Therefore it is necessary to study the time-over-threshold readout for those pulses in detail.

The aim of this chapter is to find an optimized setup for given input parameters and to point out what differentiates these setups from others. For that, the quality parameters introduced in 3.2.1, Δt , ΔQ and χ^2 , are utilized. We will follow an exemplary evaluation to present the procedure used to arrive at the concluding results; the optimized positions of thresholds in the spe region.

4.1 Parameter distributions and analysis

The starting point is a set of thresholds, a “setup”. In an example we have three thresholds set to 0.25 pe, 0.59 pe and 0.99 pe. The sampling window width is 2 ns and since we want to analyze spe pulses the mean amplitude of the generated pulses is set to 1 pe with a σ of 0.3 pe. These values result from measurements of comparable PMTs in the IceCube group in Münster when evaluating the spe peak in the charge histogram [38]. Then 60,000 generated waveforms are processed as described in chapter 3 and the quality parameters are filled into histograms, as shown in figure 4.1. These distributions give some insight of the features produced by the ToT algorithm. If we look at the ΔQ on the right side no significant deviation from a normal distribution can be observed. The entries spread around zero symmetrically with a standard deviation (σ) relative to the mean of 6.15 %. The marginal shift to negative values will be explained later when discussing a reference setup.

However, the time reconstruction on the left shows a bump at negative values in addition to a peak centered around $\Delta t = 0$. Figure 4.2 helps to

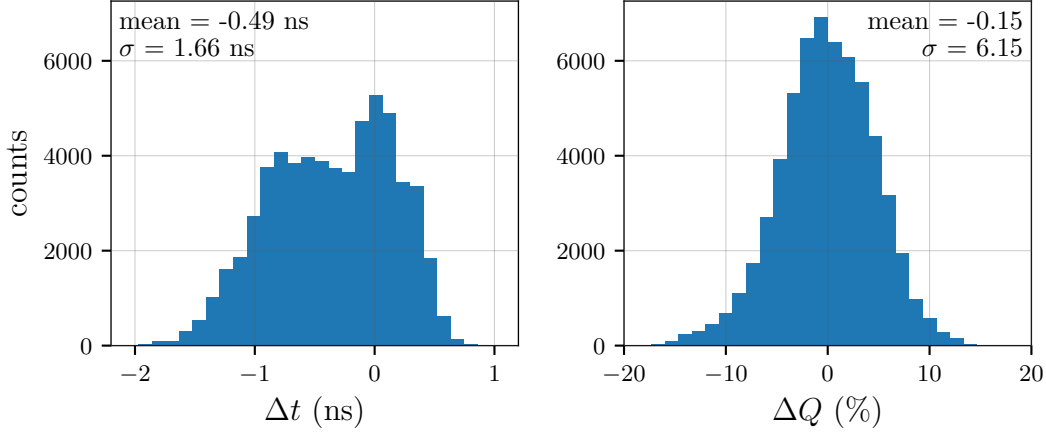


Figure 4.1: Left: Distribution of the quantity Δt after 60,000 analyzed waveforms using 3 thresholds with its mean value and standard deviation σ . Right: The ΔQ of the same data set.

identify where those entries come from. Here the Δt is resolved into bins of different total charge. We see that negative values are present for all charges yet more abundant for smaller pulse sizes. In order to find the origin of predominantly negative Δt it is instructive to plot the actual reconstructed waveforms and the original input of small total charges along with the straight lines used to find the t_0 . This is realized in figure 4.3. First, on the left, there is a case depicted in which $t_0^{true} < t_0^{rec}$ giving a positive Δt (again, the original waveform has blue colors while the reconstructed one is red). In both cases the threshold is crossed at the beginning of the sampling window meaning both sample points will be set at later times as they are set to the center of a window. That causes the whole leading edge of the pulse to be shifted back in time, as can be seen in their respective dotted lines. This kind of signatures forms the peak around $\Delta t = 0$ because their crossing of the threshold is normally distributed within a time window, around its center.

On the right side of figure 4.3, however, we see the incidences producing mainly negative values of Δt . To understand why, consider the reconstruction of a straight line that has a slope such that it runs diagonally through each sampling window. If placed randomly in time it will yield a distribution centered around zero just as discussed in the left case. But the form of the curve at the pulse's leading edge differs from a straight line such that values from the lower half lie above the diagonal and values from the upper half lie below it (compare figure 4.4, left). This means, on average, the sample points of the lower thresholds are set at earlier times and the ones of the upper thresholds are set to later times. This, in turn, results in a flatter slope for the straight line used to calculate t_0^{rec} , thus a negative Δt . For smaller maximum amplitudes this effect is even more pronounced,

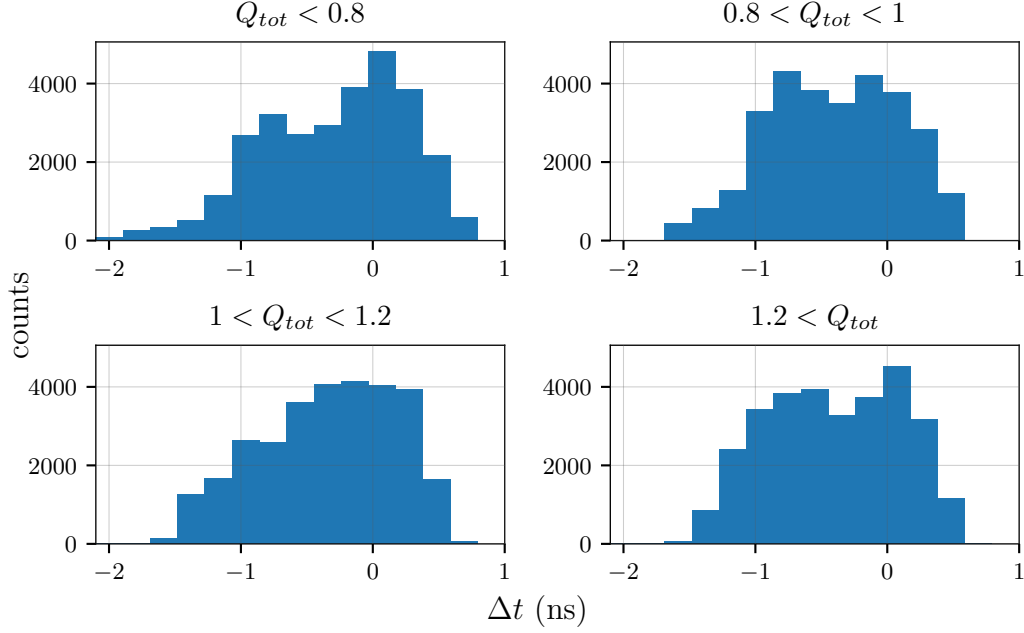


Figure 4.2: Distributions of the Δt for different regions of total charge.

explaining figure 4.2.

As part of figure 4.2 we can see that there are other, minor systematic effects of the simulation that shape the distributions. In order to find a meaningful measure whether the reconstruction worked well or not, only the mean value and the standard deviation of the distribution are considered. For the σ it is directly apparent that smaller values are desirable; they correspond to a more reliable procedure. For the mean value, though, it has to be checked if there are systematic influences that intrinsically cause a shift, as one might expect in the case of the Δt in our example, or whether this a real feature of this specific setup. If the first proves to be true a fixed offset for the analysis (and the actual realization) would have to be incorporated.

To assess this a reference setup is used consisting of 80 thresholds 0.025 pe apart (up to a maximum of 2 pe). The sampling width has been set to as low as 0.25 ns. This should inherently rule out systematic effects. The result is shown in figure 4.5 giving the answer to the question posed before: There is no considerable offset in any of the mean values as even the Δt is centered around zero. Instances responsible for the tail of negative entries in ΔQ share that the points close to the maximum spend a considerable time in between two thresholds so that many sampling points with less weight had to be set half way (see figure 4.4, right). This causes a lower maximum amplitude and thus less Q_{tot}^{rec} . It becomes explicitly visible here but is also present in the ΔQ distributions before causing, for example, the negative mean in figure 4.1.

The same is carried out examining the quantity χ^2 with the results

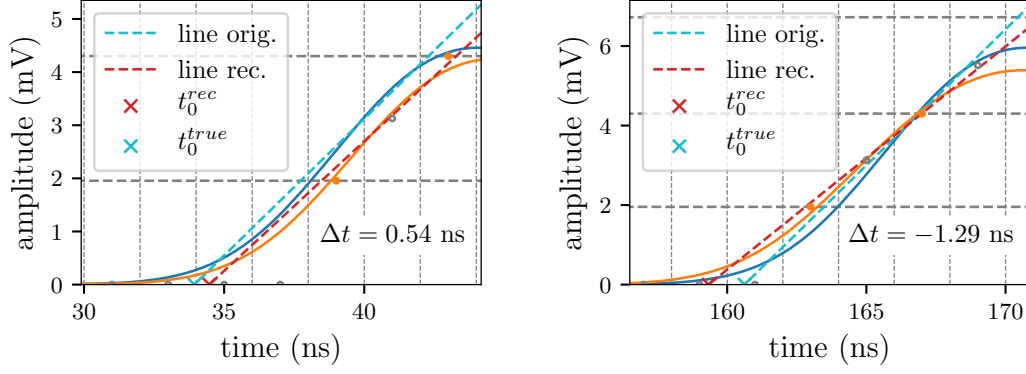


Figure 4.3: Left: Scenario contributing to the peak around zero. Right: Instances adding to negative Δt caused by the shape of the curve relative to the sampling windows.

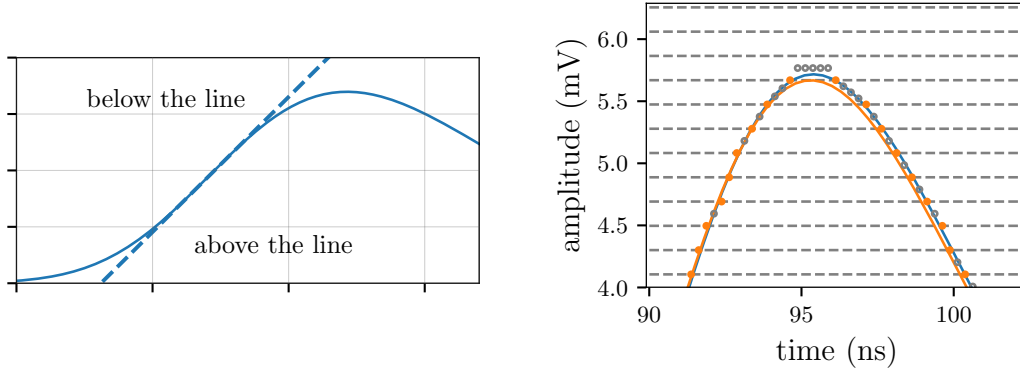


Figure 4.4: Left: Explanation for negative Δt . On average, sample points are set further to the left than the straight line for small amplitudes and further to the right for bigger amplitudes. Right: Instances causing slightly lower Q_{tot}^{rec} in the reference setup.

shown in figure 4.6. The histogram on the left is again the distribution for 60,000 analyzed waveforms using the three-threshold example setup with a sampling width of 2 ns and the one on the right uses 80 thresholds and 0.25 ns sampling width. This quantity is, as expected, not prone to systematical effects indicated by smooth distributions in both cases.

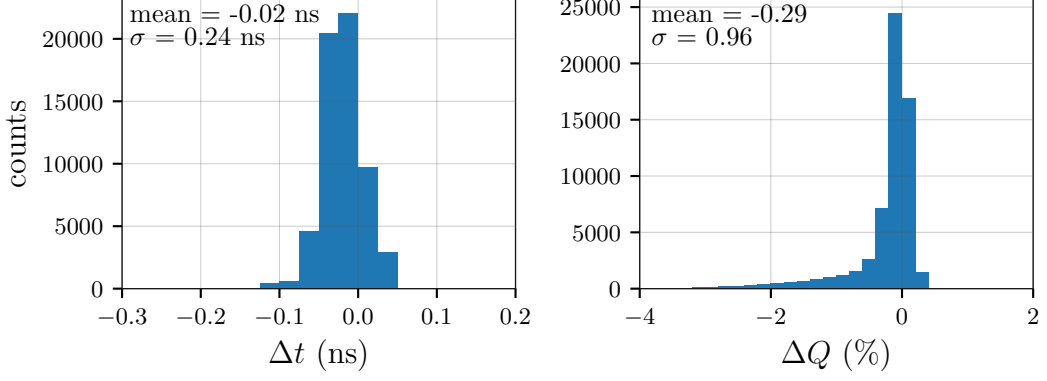


Figure 4.5: Distributions obtained by a reference setup using 80 thresholds and 0.25 ns sampling width. Δt left and ΔQ right.

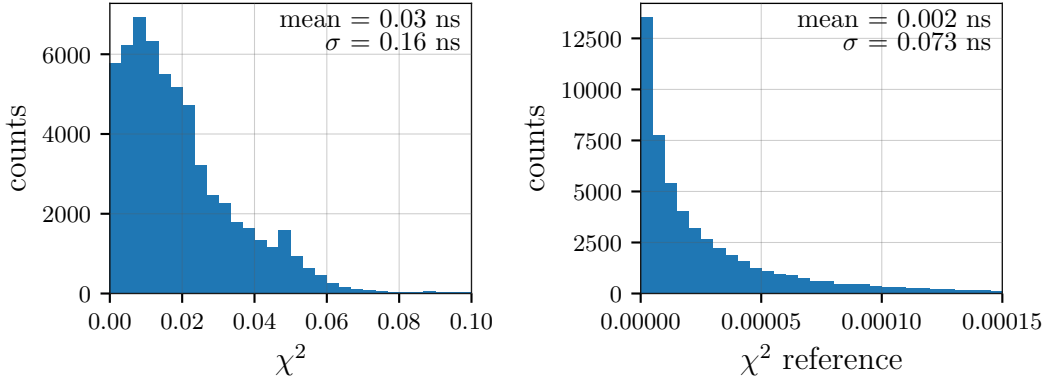


Figure 4.6: Distributions to investigate systematics in χ^2 . Left: The example setup with three thresholds. Right: The reference setup.

4.1.1 Parameter behavior for large numbers of iterations

Having mentioned that mean and standard deviation of the distributions will be used for further analysis let us take a look at how they behave with increasing number of processed waveforms. In order to make the studies efficient, we need to find a good compromise between analyzing sufficiently many waveforms for reliable results and invested computation time. Therefore in figure 4.7 the discussed quantities are plotted versus the number of iterations. It indicates that after about 10,000 processed spe pulses all parameters are sufficiently close to their asymptotic value making this the number used in the following studies.

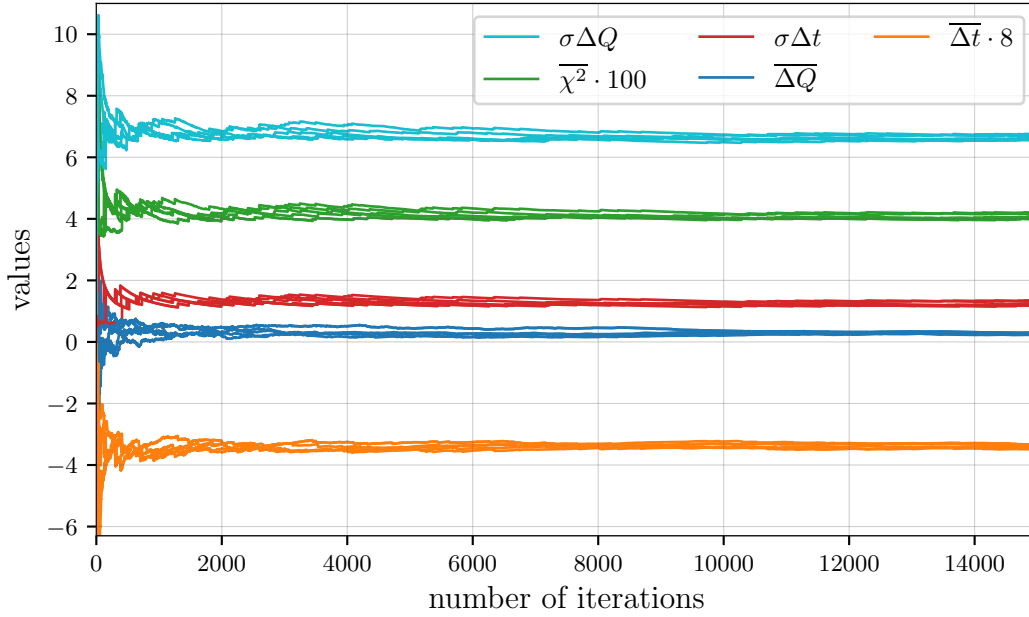


Figure 4.7: Behavior of the quality parameters as a function the number of processed spe pulses. The value of χ^2 has been scaled by factor 100 and mean Δt by 8 for better visibility.

Now that we have a measure for the reconstruction quality at our disposal we can test different setups and use the parameters to filter them by applying cuts. The method to determine the best performing ones is subject to the next section.

4.2 Method and results of optimization

In order to be able to test all reasonably possible setups, the amplitude of each threshold involved is varied independently of one another across a certain region. The only limitations here are that the lowest threshold is always fixed to 0.25 pe and that the highest threshold does not surpass 2 pe as this is too far beyond the spe region. Apart from that, the adjustable thresholds are set to all combinations in between with a binning of 0.02 pe, always preserving their order.

To clarify this procedure the example of three thresholds helps us again: The second and third threshold start at 0.27 pe and 0.29 pe, each one in the next free position, directly above the first, fixed threshold. Then the third is moved gradually all the way up to 2 pe. After that, the second is moved 0.02 pe up and threshold three is varied again.

We will consider the cases of 2 to 5 thresholds used to sample a spe pulse. As mentioned before, alternating the position of one single threshold does not make sense for the actual setup as it is needed to be the noise threshold at 0.25 pe. Nevertheless, it provides the possibility to check the robustness of the method as we can expect a distinctly preferred amplitude providing the best results. At the other end, varying more than five thresholds simultaneously demands considerable computing time while five thresholds already cover the spe region relatively well considering the rest of the dynamic range.

4.2.1 Cuts in time and charge and characteristics of their results

The data obtained from parallel processing using a computing grid consists of the mean and the standard deviation of Δt and ΔQ , and the mean value of χ^2 from 10,000 processed waveforms along with the positions of the thresholds for each setup.

For the analysis, three classes of setups are defined with increasing demands for the four physical parameters. Let us follow again the example of three thresholds active. Figure 4.8 contains the four parameters and also shows the classes compared to the data from all threshold combinations. Cuts are performed simultaneously in the standard deviation and the mean value of both Δt and ΔQ to determine setups that have the least spread in time and charge and a mean value closest to zero. Here, the boundaries are more strict on the mean value than on the standard deviation. To get a feeling for it, the precise numbers for the three-threshold example are listed in table 4.1.

Using several classes instead of only looking for the best results allows

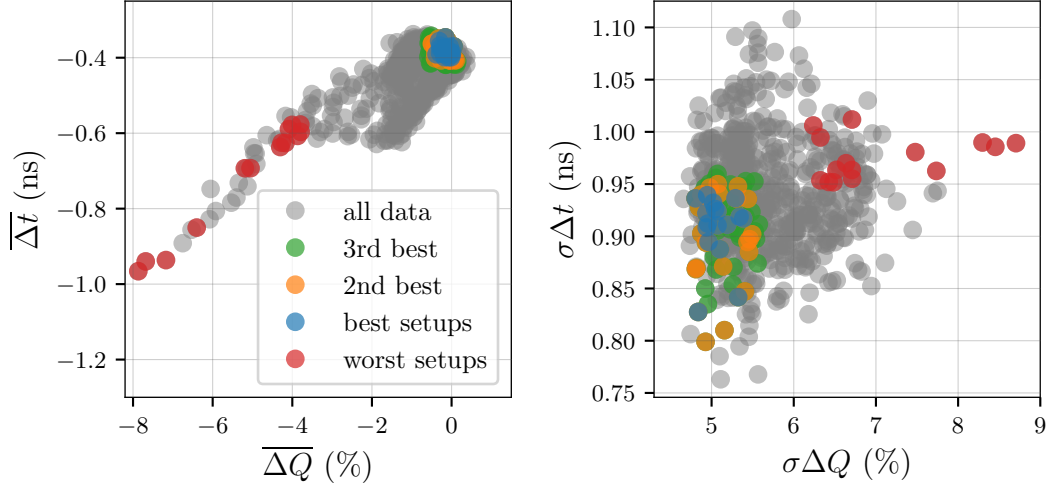


Figure 4.8: Plot of mean (left) and σ (right) of Δt and ΔQ of all data obtained from the variation of threshold positions. Highlighted with colors are the filtered setups after cuts.

Table 4.1: Cut boundaries for 3 thresholds.

class	$\overline{\Delta Q}(\%)$	$\overline{\Delta t} \text{ (ns)}$	$\sigma \Delta Q(\%)$	$\sigma \Delta t \text{ (ns)}$
1	0.4	0.4	5.4	0.94
2	0.5	0.41	5.5	0.95
3	0.6	0.42	5.6	0.96

to screen for consistency; as we will look at some characteristics of the setups in the next plots the behavior between classes is not expected to change dramatically. Additionally badly performing setups are marked also which should, in turn, have significantly different properties.

First of all, there is a representation of the determined amplitudes yielding the best reconstruction in figure 4.9. For that, the amplitudes of all classes are filled into a histogram and weighted by importance. The first class (blue), consisting of the best performing setups, is weighted by 1, the second class by 0.2 and the third class by 0.05. Note that class 1 is contained in class 2 and class 2 in class 3 which causes the small weighing factors for classes 2 and 3. Included is also the first threshold, which is, as mentioned before, always set to 0.25 pe, to visualize the ratio each class has after weighting. The fitted Gaussian distributions give the optimal positions and are listed in table 4.2. The uncertainty is given by the σ of the Gaussian distribution except for the special case of one threshold where it is the FWHM (explanation see later).

For each number of thresholds a distinct most favorable position can be derived making this an important result of this thesis.

The trend that can be observed is that with increasing number of

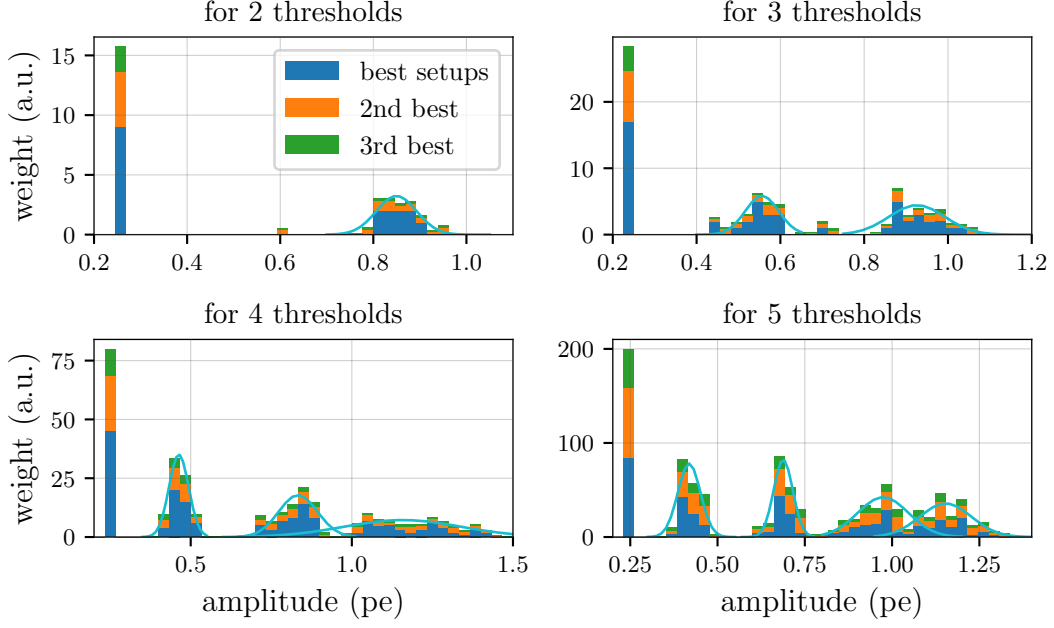


Figure 4.9: Threshold position of the best performing setups. Fitting the clustered entries gives the optimal position. Also included is the lowest, fixed threshold.

Table 4.2: Optimal positions for each number of thresholds in pe.

# of thrs.	first	second	third	fourth	fifth
1	0.21 ± 0.05				
2	0.25	0.85 ± 0.04			
3	0.25	0.56 ± 0.04	0.93 ± 0.06		
4	0.25	0.46 ± 0.03	0.83 ± 0.06	1.16 ± 0.18	
5	0.25	0.42 ± 0.03	0.69 ± 0.03	0.97 ± 0.07	1.15 ± 0.07

thresholds involved the available range is approximately evenly divided. The maximum amplitude covered rises up to 1.15 pe. The two observations imply that if more thresholds than five are utilized for covering spe pulses they are best distributed evenly between 0.25 and 1.15 pe.

Figure 4.10 shows the maximum amplitudes in more detail. They are smooth distributions around an optimal value except for the case of four thresholds. Here the amplitude varies significantly between 1 and 1.4 pe with two formed maxima. It was not possible to identify the cause of it not even by varying cut boundaries. Other effects that contradict robustness of the method are marginal; in the case of two thresholds a few entries suggest the best position for the second position around 0.6 pe and with tree thresholds the third class has a maximum shifted by 0.1 pe compared to the one formed by first and second class setups.

As a verification, the obtained setups should be among the ones with

the smallest value of χ^2 . This comparison is shown in figure 4.11. Here the setups found with the method above are marked in color against the grey background of all possible combinations of amplitudes. In agreement with the physical quality parameters, the selected setups have low χ^2 and therefore are valid candidates for an optimized sampling of spe pulses. The previously deemed worst setups also rank between the ones with the highest χ^2 values.

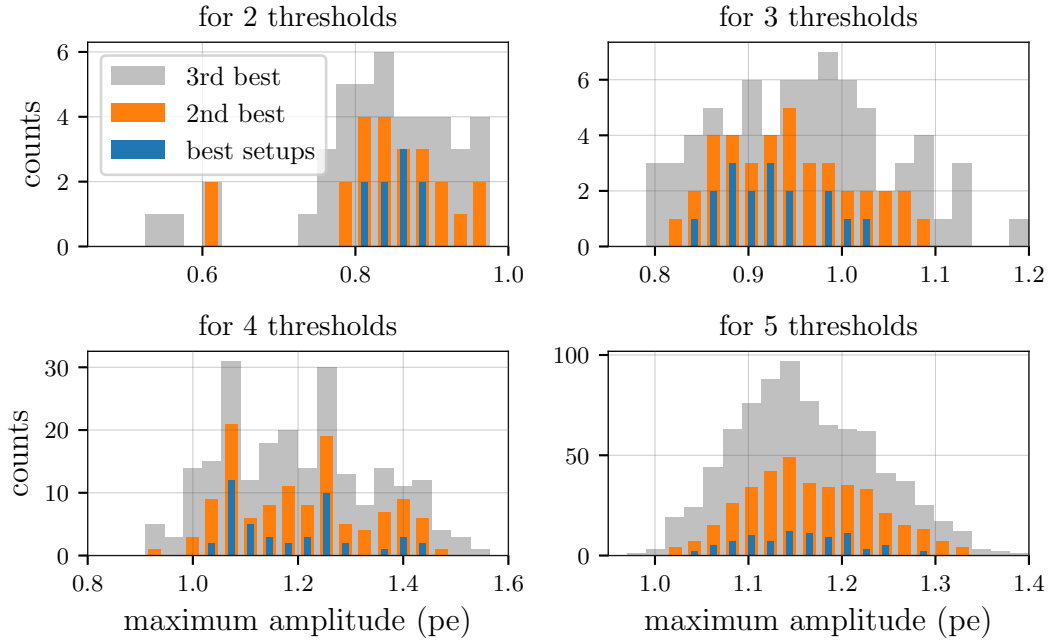


Figure 4.10: Detailed view of the maximum amplitude for two to five thresholds. The distributions generally spread around one distinct mean amplitude.

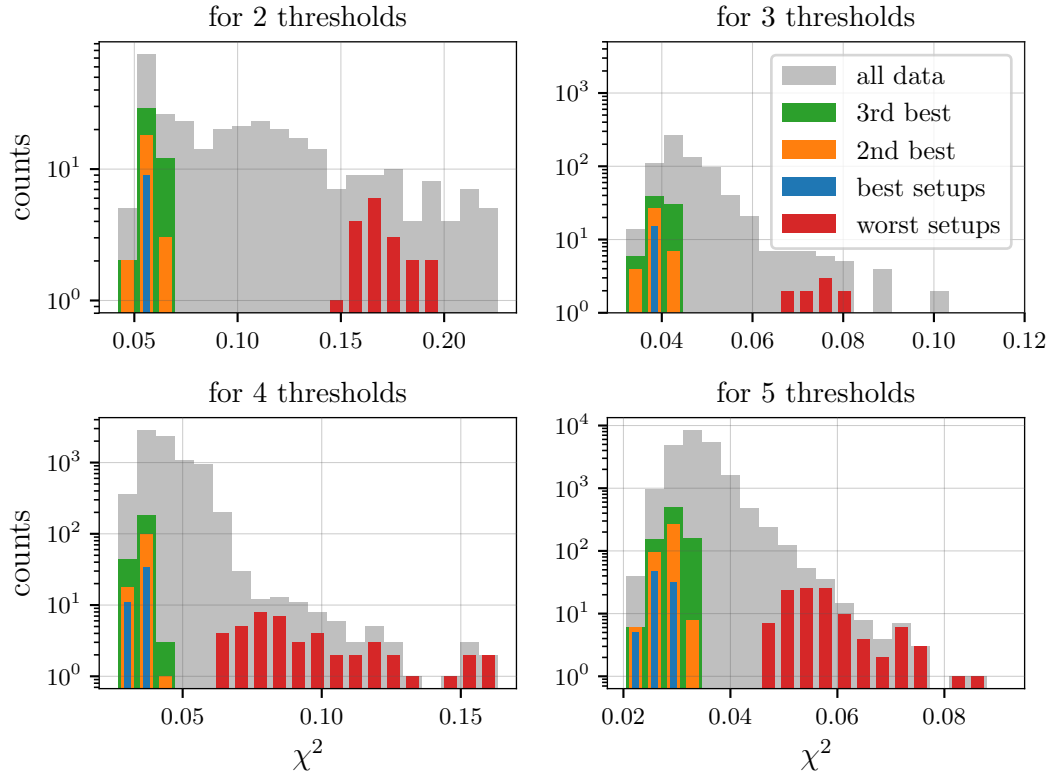


Figure 4.11: The χ^2 distributions for two to five thresholds. The filtered setups are highlighted again and prove to be consistent as well performing setups rank among the smallest χ^2 .

Previously, it was indicated that varying the position of a single threshold allows checking for consistency. The results of the optimization are shown in figure 4.12. On the left the χ^2 distribution is shown including the filtered classes; again it proves to be consistent with the cuts made in mean and standard deviation of Δt and ΔQ . The plot on the right shows the optimized position. This time it is fitted by a ninth-degree polynomial to account for the asymmetrical shape. Hence the full width at half maximum is given in table 4.2 as its uncertainty. With 0.21 pe this is close to the anticipated noise threshold of 0.25 pe making the result a compatible candidate for an implementation of a single threshold covering the spe region.

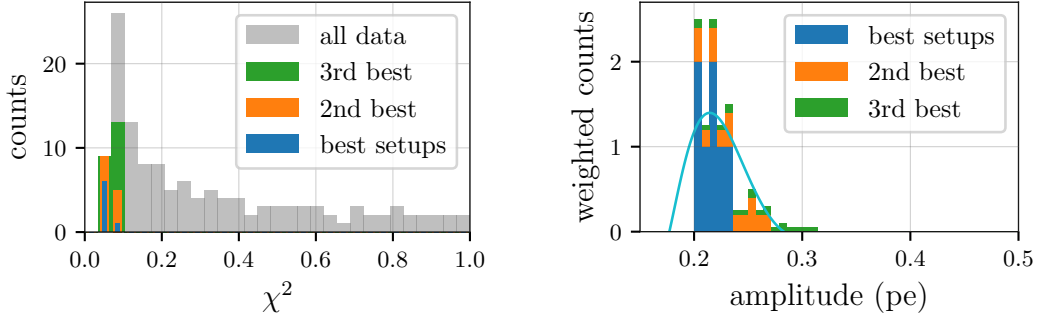


Figure 4.12: Analysis of the performance of a single threshold sampling the waveform. Left: The result after cuts with the optimal amplitudes. Right: The χ^2 distribution for consistency checks.

Concluding this section is an overview comparing the best setups from each number of thresholds presented in figure 4.13. For better visibility, the means of the distributions are marked in silver.

Considering the charge reconstruction no unexpected behavior can be observed; the more thresholds are used the closer the mean value is to zero and the smaller the σ of the distribution. The first class of five thresholds leads with mean values around -0.1% and a σ of about 3.8% . One threshold performs considerably worse with $\overline{\Delta Q} = -2.7\%$ and a spread of more than 10% .

But for the time reconstruction using a single threshold yields more precise results than any other while having a low σ around 0.8 ns comparable to that of 5 thresholds. This can be explained by the fact that only one sampling point is created and thus no systematic effects from positions inside a sampling window play a role. This was identified in chapter 4.1 to be the reason for the shape of the Δt distribution and its negative mean

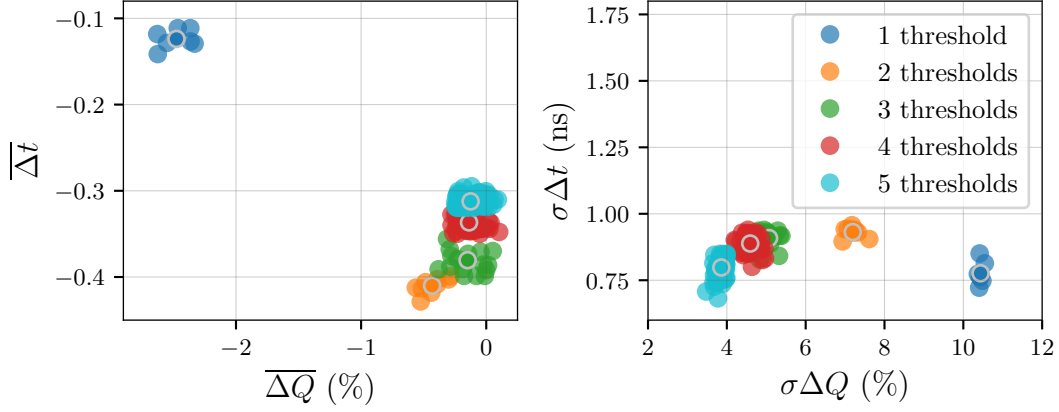


Figure 4.13: Comparison of the performance of different numbers of thresholds active. The mean value of Δt and ΔQ is plotted on the left, the σ on the right. In silver the center of the cluster is highlighted.

value. Two to five thresholds rank again in the expected order in both mean and σ of Δt .

Considering the temporal resolution of PMTs in the order of 3 – 4 ns [39] shifts of less than 1 ns are a rather small effect. Nevertheless additional aggravation is to be avoided which is why the quantity Δt is still considered for optimization.

4.3 Influence of the sampling window width

So far a fixed sampling window width of 2 ns has been used for all simulations. In this section the value is varied and the quality parameters are evaluated again. This time an exemplary setup of four thresholds (0.25, 0.47, 0.77, 1.05 pe) has been chosen while other numbers of incorporated thresholds yield the same results qualitatively. For Δt and ΔQ the dependence on the sampling width is shown in figure 4.14. On the left, the $\overline{\Delta t}$ shows expected behavior; the longer the time windows the more pronounced becomes the effect causing negative values. The standard deviation is not affected by a change in sampling width further supporting the fact that there is no other significant systematic effect present apart from the one discussed.

For ΔQ the σ rises slightly with larger windows while the mean value shows no significant shift from zero. This is also in accordance with the described effect as the distribution of ΔQ is not shaped particularly by sampling windows. The σ increases simply because there are fewer sample points available causing a larger spread.

Additionally, a plot for the χ^2 is shown in figure 4.15. It also exhibits

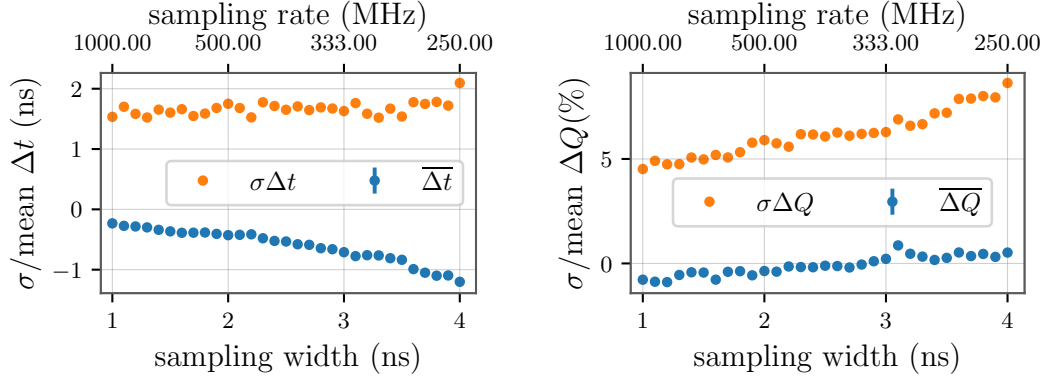


Figure 4.14: Influence of the sampling window width (sampling rate) on the quality parameters. Left: Mean and σ of Δt . Right: Mean and σ of ΔQ .

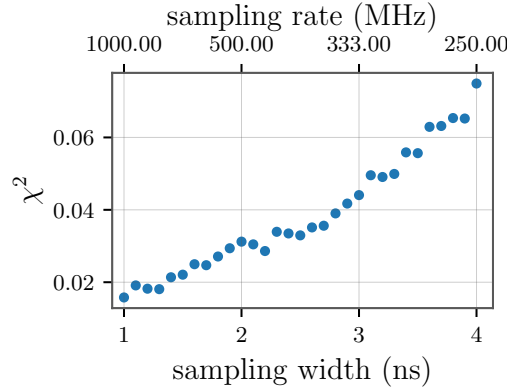


Figure 4.15: Influence of the sampling window width on the χ^2 .

the same feature as just discussed: The larger the sampling window width is, the less similar the two waveforms are as reconstruction gets worse due to less information sampled from the original input.

4.3.1 Influence of real data features

Before we move on to analyzing real data let us try to predict what we can expect for the parameters using the simulation program. The bin width of the ATWD, providing the waveform, is 3.33 ns and thus this value is also used as bin width of the reconstructed waveform and as sampling window width. Setting these values for the simulation yields the distributions in figure 4.16. As the bin width and sampling width increases, the systematic effects become more pronounced and Δt shifts further to towards lower values from -0.49 ns in the example before to -0.62 ns. The σ of both distributions also increases slightly. With noise occurring we would expect

the real data to show an even larger σ . In the next chapter, we shall see what the actual result is.

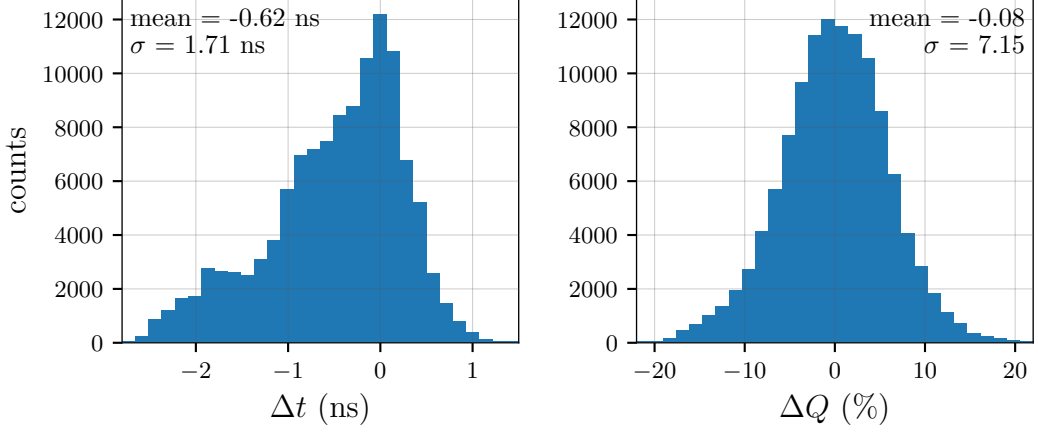


Figure 4.16: Distributions for Δt (left) and ΔQ (right) for a setup of three thresholds with a waveform binning of 3.33 ns and the same sampling window width for better comparability to the analysis of real data in the following chapter.

5 Analyzing real data and performing direction reconstruction

IN this chapter waveforms from real IceCube events serve as input for sampling and reconstruction of pulses. First, we look at how well this data is processed by evaluating again the known parameters Δt , ΔQ and χ^2 for different setups. This helps us understand what additional effects come into play when working with signals containing noise. Furthermore, IceCube's standard direction reconstruction for cascades is executed for the case of ToT pulses and the performance of different setups is compared.

5.1 Creating ToT pulses from real IceCube data

In chapter 3.3 it was mentioned that some minor modifications had to be applied to the ToT algorithm to provide valid results using real data as input. Apart from that, the waveform is processed the same way as in the standalone simulation.

The actual dataset consists of 76 high-energy starting events offering a wide range of total charge detected in one DOM. Next to a majority of single photoelectron pulses some waveforms contain more than 200 pe. Every event is analyzed entirely by looping over the DOMs of all strings. The output is twofold: On the one hand there are the values for Δt , ΔQ and χ^2 for each waveform. On the other hand reconstructed pulses created with the ToT algorithm are saved to an *I3File* to be used in the direction reconstruction.

The experimental statement of requirement provides to use 4 or 64 thresholds (see chapter 2.4) for covering the whole dynamic range. The possibility of 16 thresholds was also discussed. For the purpose of determining the optimal threshold positions for the mDOM analyzing existing DOM data, it is more reasonable to use 16 thresholds given the lower dynamic range of the DOM which is limited by saturation to a maximum amplitude of 120 mV. Though closer to the actual experiment,

64 thresholds would cover the signal very well in almost any constellation. Hence, to demonstrate the contrast between different setups more distinctly 16 thresholds have been chosen for testing the sampling in this thesis.

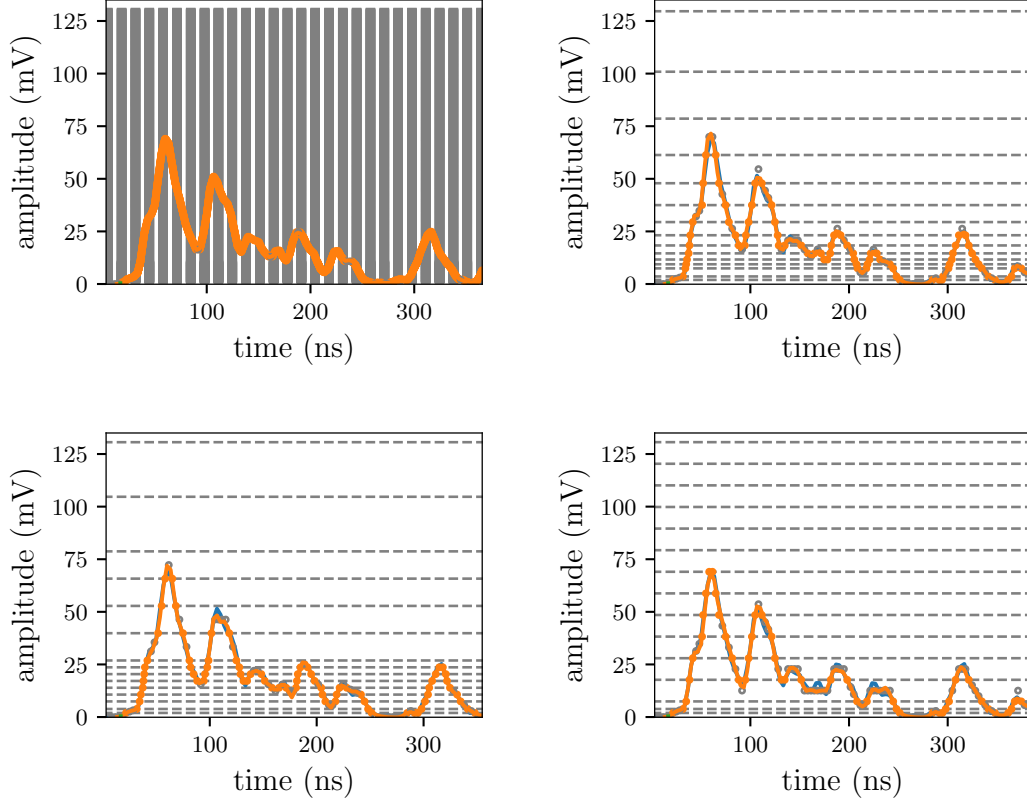


Figure 5.1: Overview of the four setups used while sampling an exemplary waveform. Top left: Reference. Top right: Exponential. Bottom left: Semi-exponential. Bottom right: Linear. Note that the reference setup consists of overall 600 thresholds densely spaced and are thus hardly resolved as single lines in this representation.

There are three different setups used for comparison as well as a reference setup which is again supposed to give a near perfect reconstruction allowing to screen for systematic offsets. The four distributions of threshold positions are shown in figure 5.1. As its name suggests the “exponential” setup has thresholds set at exponentially increasing distances. However, the spe region is covered by thresholds at 0.25, 0.56 and 0.93 pe as this was the result of the preceding studies of chapter 4 and already the optimal combination for this region if three thresholds are used. This is also the case for the “linear” setup which uses equally spaced thresholds from 0.93 pe on. As a means of checking for consistency a “semi-exponential” setup should

always show results that stay within the limits set by the exponential and linear one. It has, beyond the spe region, three different blocks of thresholds increasing in distance and decreasing in number with amplitude yielding overall groups of 3 (spe region), 7, 4 and 2 thresholds. The chosen semi-exponential setup is a quite close approximation of an exponential distribution which implies that it should behave more similar compared to the exponential one than to the linear. Lastly, the reference setup starts at 0.1 pe amplitude, uses 100 thresholds up to 1.1 pe and another 500 for the rest of the dynamic range.

The first result presented will be the answer to last chapter's consideration about how the spe region is sampled by the ToT algorithm in real data. Figure 5.2 has the same distributions plotted as in figure 4.16 for total charges smaller than 1.4 pe. In Δt , we observe roughly the same shape with

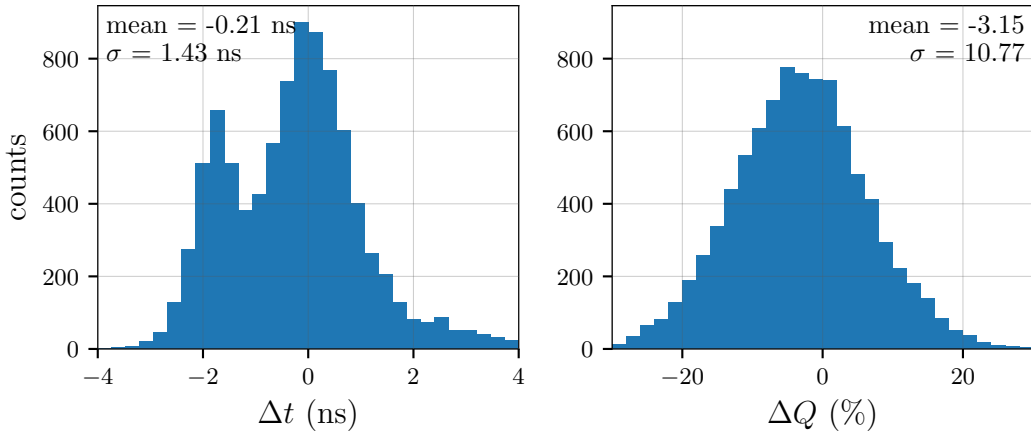


Figure 5.2: Distributions for Δt (left) and ΔQ (right) for a setup of three thresholds sampling real data (3.33 ns sampling width). Only waveforms featuring a total charge of less than 1.4 pe are considered.

a maximum around -2 ns as it was present in the simulated input. There are now several more entries for positive values shifting the mean further towards higher values than it was the case in the simulation ($\overline{\Delta t} = -0.21$ ns and -0.62 ns, respectively). As for the standard deviation, the value for Δt is smaller in real data, while it is larger for ΔQ than predicted in the last chapter. Also, the mean value for ΔQ is shifted to negative values. We will look at some explanations for this in the following section but, for the time being, it can be stated that no unexpected, considerably different behavior can be observed when going over from simulation data to analyzing actual events.

5.1.1 Evaluating setups over the whole dynamic range

Following the approach of consulting the quality parameters Δt , ΔQ and χ^2 the reconstruction performance for different bins of total charge is studied in this section. First, $\overline{\Delta Q}$ is shown for the four selected setups in figure 5.3. The uncertainty is given by the standard error of each charge bin. The standard error e gives the uncertainty of a mean \bar{x} with standard deviation σ for a sample size of N : $e = \sigma/\sqrt{N}$.

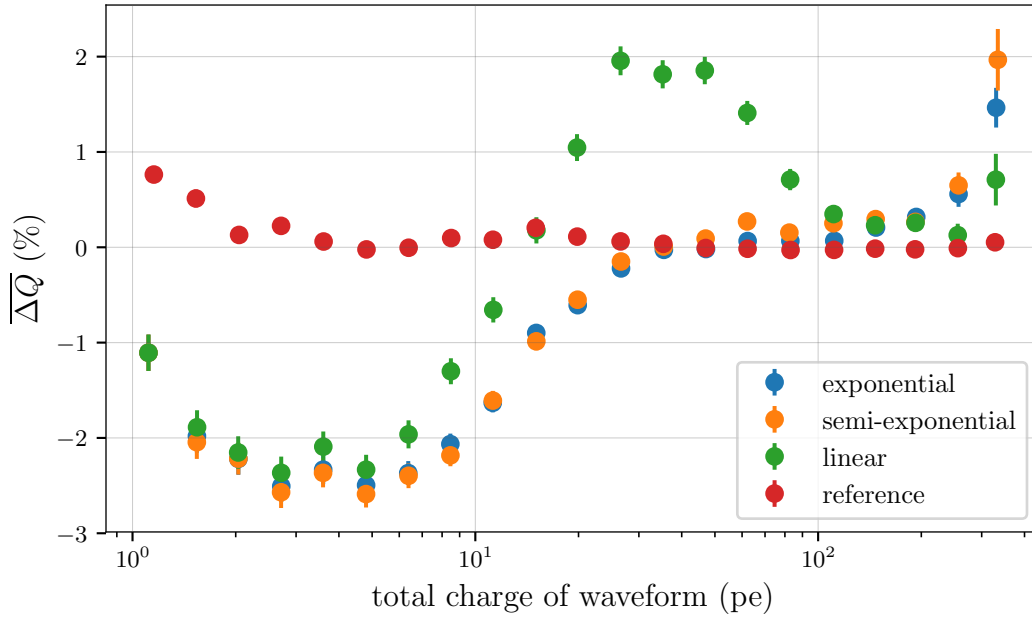


Figure 5.3: $\overline{\Delta Q}$ as a function of the total charge contained in a waveform for the four considered setups.

It becomes apparent that the reference setup does not show any considerable deviation from the zero line for almost the entire range. Only for small total charges it becomes slightly positive. That implies, as $\Delta Q \propto Q_{tot}^{rec} - Q_{tot}^{true}$, more charge is measured in the reconstructed waveform. This marginal effect is due to the baseline of the original signal, which fluctuates around zero while the reconstructed pulse is smooth (see 5.4, top left). This has already been addressed at the end of chapter 3.3 where the fix was to minimize the considered region for calculation. Yet, this deviation is the remaining influence of this effect.

In contrast to that, all other setups show larger true charge compared to the reconstructed one. This, in turn, can be explained by the fact that a few signals do not reach the lowest threshold and are thus not sampled at

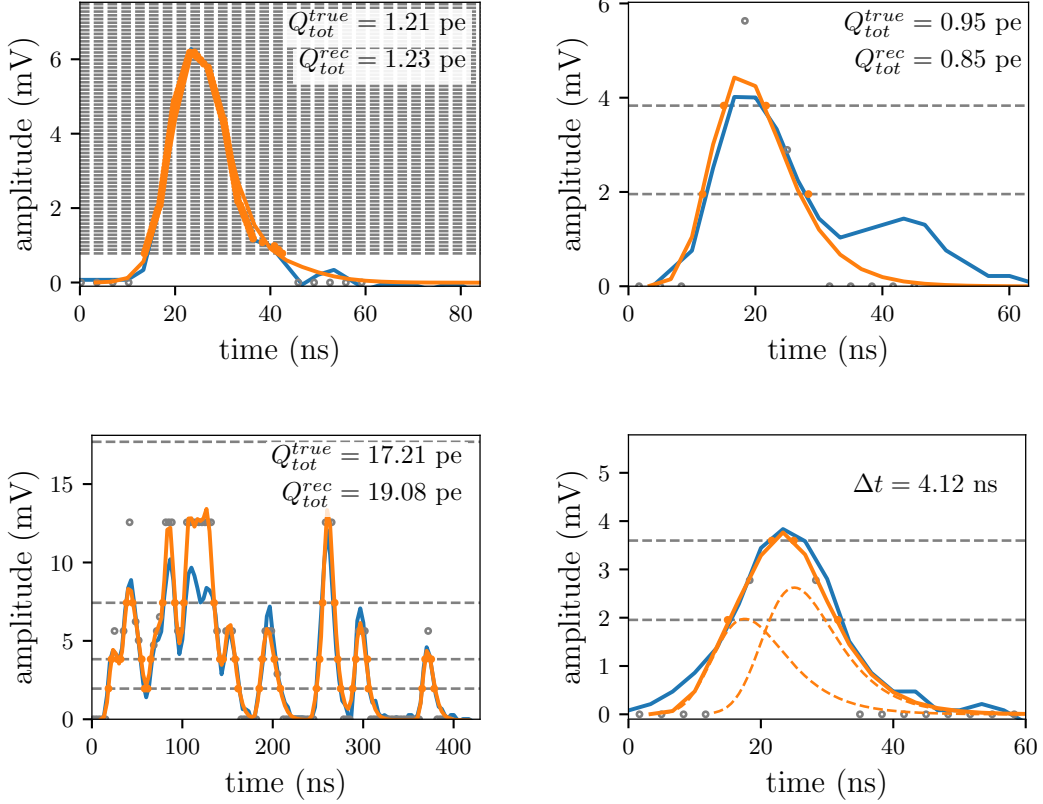


Figure 5.4: Examples to illustrate the effects responsible for shaping the behavior of the charge and time reconstruction. The original waveform is displayed in blue while the reconstructed one is orange. Top left: Larger reconstructed charge in the reference case due to noise fluctuation. Top right: Smaller reconstructed charge due to small signals in the true waveform. Bottom left: High distance to the first threshold beyond the spe region for the linear setup. Bottom right: Case depicting $t_0^{rec} > t_0^{true}$.

all. However, when they occur inside the time window of a sampled pulse they are considered for calculating the charge difference (example shown in 5.4, top right) and result in negative ΔQ . This is consistent with the fact that the effect becomes less pronounced with increasing total charge.

The first physically relevant difference between the setups is observable in the region from 20 to 80 pe total charge. Here the linear distribution of thresholds yields less accurate results than the exponential and semi-exponential distributions. This is to be expected as thresholds right above the spe region are very sparse in the linear case compared to the other setups and hence cannot sample these signals very well. Figure 5.4, bottom left, shows an illustration of that. The more charge is contained in the waveform, the better the linear distribution of threshold performs. After a transient from around 100 to 170 pe, where all setups are more or less aligned, the linear setup yields considerably better results for charge reconstruction due to its denser spacing in the upper end of the dynamic

range compared to the exponential and semi-exponential setup. However, the statistics are not very high, even among the HESE, resulting in large uncertainties.

The same explanations hold true when plotting the σ of ΔQ and the χ^2 . Figure 5.5, left, shows the latter distribution while the former is qualitatively the same. One additional feature becomes visible here: The semi-exponential setup stays between the limits of the linear and exponential distributions for most bins underlining robustness of the results.

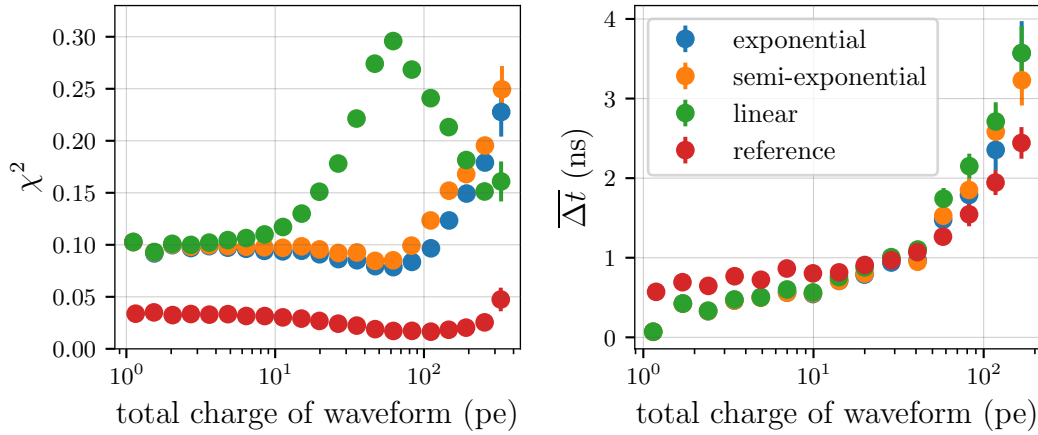


Figure 5.5: Mean of the χ^2 distribution (left) and $\overline{\Delta t}$ (right) for different total charge contained in one waveform.

The $\overline{\Delta t}$, presented in figure 5.5 on the right, shows positive values for all charges, increasing in absolute value towards larger waveforms. This contradicts the statement from the beginning of the chapter, claiming negative $\overline{\Delta t}$ for small spe pulses. When examining concrete cases with high Δt , it becomes apparent that often the first pulse in a waveform seems to start off earlier then predicted in the pulse template used for fitting. One incident is shown in figure 5.4, bottom right. The shallow rise for the original waveform in combination with the steep ascent of the reconstructed pulse leads to a large, positive Δt . This effect is more pronounced for larger waveforms and is also accompanied by an increase in the standard deviation plotted on the left of figure 5.6. Since the reference setup shows a similar behavior the offset is subtracted as shown in figure 5.6, right. For small waveforms we recognize the negative values around $\overline{\Delta t} = -0.5$ ns. For waveforms containing more than 10 pe the discussed effect takes over for the exponential, semi-exponential and linear setup causing positive $\overline{\Delta t}$.

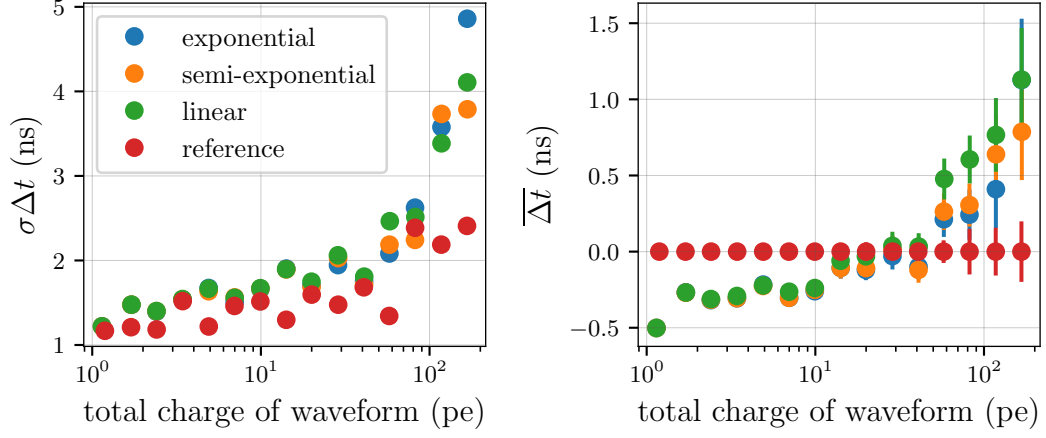


Figure 5.6: Left: Standard deviation of Δt versus the total charge in a waveform. Right: $\overline{\Delta t}$ normalized to the offset of the reference setup.

This said, the introductory plot 5.2 was already corrected to the positive offset in $\overline{\Delta t}$.

5.2 Performance testing: Direction reconstruction on ToT pulses

Another possibility to test the quality of the obtained ToT pulses is to use them for direction reconstruction. With this, the incident direction of the interacting neutrino and thus its coordinates in the sky are determined.

5.2.1 Direction reconstruction in IceCube

In this thesis, IceCube’s existing direction reconstruction for cascades is taken and slightly modified. Therefore the concept of the reconstruction will be introduced.

The general idea of it is to test all angle combinations representing a point in the sky for the likelihood that the detected particle actually originated from that direction.

In the first step, initial guesses for the vertex position inside of the detector and the vertex time are made. The former is simply calculated to be the charge-weighted average position of the first hit DOMs while the latter is defined to be the time of when the total number of photons detected surpasses a certain threshold.

Next, a grid of the whole sky is created with the help of the algorithm HEALPix [40] which divides the surface of a 2-dimensional sphere into segments of equal area. For each of these “pixels” an *I3Particle* inside the IceTray framework is generated. Its properties are: The type (cascade in this case), zenith and azimuth angle as the incoming direction, the vertex position and time from the initial guess and an unspecified energy which will be determined as part of the fit. The position is slightly varied by creating more particles with offsets in all three spatial dimensions but otherwise identical properties.

The deposited energy of the interacting particle is proportional to the number of detected photons. Thus, tables containing ice properties are used to compute the energy for a given input of incident photons and their position in the ice.

For the actual fit, all pulses of all DOMs are considered. Each waveform is sliced into time bins that contain 15 pe maximally. For every bin an expectancy provided by the hypothesis particle is determined. Using this and the actually recorded pulses a Poisson likelihood (LH) from all bins is calculated. This quantity is then minimized yielding the likelihood for the selected direction and the energy as products. This is repeated a second time taking the values found in the first pass as initial guesses, including the energy.

After all pixels of the grid are treated this way, a sky map of likelihoods

can be plotted. As the output is given by $-\log(LH)$ the smallest values correspond to the most likely direction of the neutrino (see for example figure 5.8).

The uncertainty for this direction is consequently defined via the change in likelihood. The so-called Wilks' theorem [41] predicts that for a null hypothesis (index 0) and an alternative hypothesis (index t) the test statistic $2(\log(LH_t) - \log(LH_0))$ is $\chi^2_{dof}(x)$ distributed with degrees of freedom (dof) equal to the difference in free parameters between the two hypothesis. The dof in this case is 2 for θ and ϕ . LH_t is the likelihood of a considered point while LH_0 represents the maximum likelihood. Note that here the term $\chi^2_{dof}(x)$ refers to the actual mathematical distribution of which the cumulative distribution function is depicted in figure 5.7 and not to the definition given in equation (3.3).

To shed some light on this definition let us consider an example, where the likelihood sky map is given and a maximum can be identified. This is our null hypothesis and has $-\log(LH_0) = 2380$. All other points (alternate

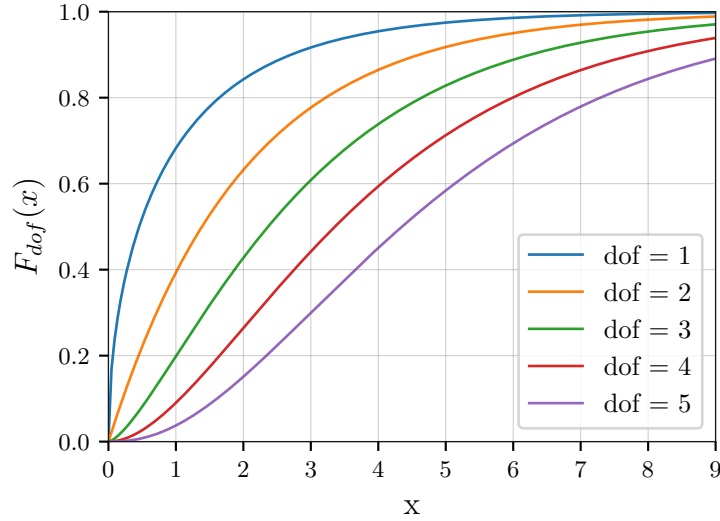


Figure 5.7: Cumulative distribution function of χ^2_{dof} for different dof . $F_{dof}(x) = \frac{1}{\Gamma(k/2)}\gamma(\frac{k}{2}, \frac{x}{2})$ where Γ is the gamma function and γ the lower incomplete gamma function. For $dof = 2$ this simplifies to $F_2(x) = 1 - e^{-x/2}$.

hypothesis) differ by the difference in likelihood $D_t = \log(LH_t) - \log(LH_0)$. For the point t_1 with $-\log(LH_1) = 2383$ it follows that $D_1 = 3$. The theorem tells us this quantity follows the cumulative distribution function of χ^2 with $dof = 2$, namely $y = \chi^2_2(2D_1)$. The y is directly connected to the confidence level (CL). If an experiment is repeated a number of times and a mean value is calculated, a CL of for example 90 % states that in

90 % of the cases the true value is contained within the limits around the mean set by the confidence interval.

For our example case of $y = \chi^2_2(2 \cdot 3)$ we get $y = 0.95$ (see figure 5.7). This means that the probability to contain the true direction in an area of 3 units around the maximum in the $\log(LH)$ space is 95%.

By starting off with a confidence level of 90% ($y = 0.9$) we compute $x = 4.61$ and thus $D = 2.305$ to use this as the limits in the $\log(LH)$ space. Since this is commonly used in IceCube it will be also the measure of uncertainty in the following.

Direction reconstruction is one major topic in IceCube as one aim of the experiment is to identify point sources of neutrinos. The result of the ongoing study has been shown in the introduction (figure 2.8) and marks one major achievement of the collaboration so far.

5.2.2 Determining the incident direction

The method employed to determine the maximum in the likelihood space was optimized to not use extensive computing time while still yielding reliable results. Thus three steps are executed in succession: First, the whole sky is scanned by the standard direction reconstruction on the ToT pulses utilizing a sparse binning (see figure 5.8). This gives a first idea of

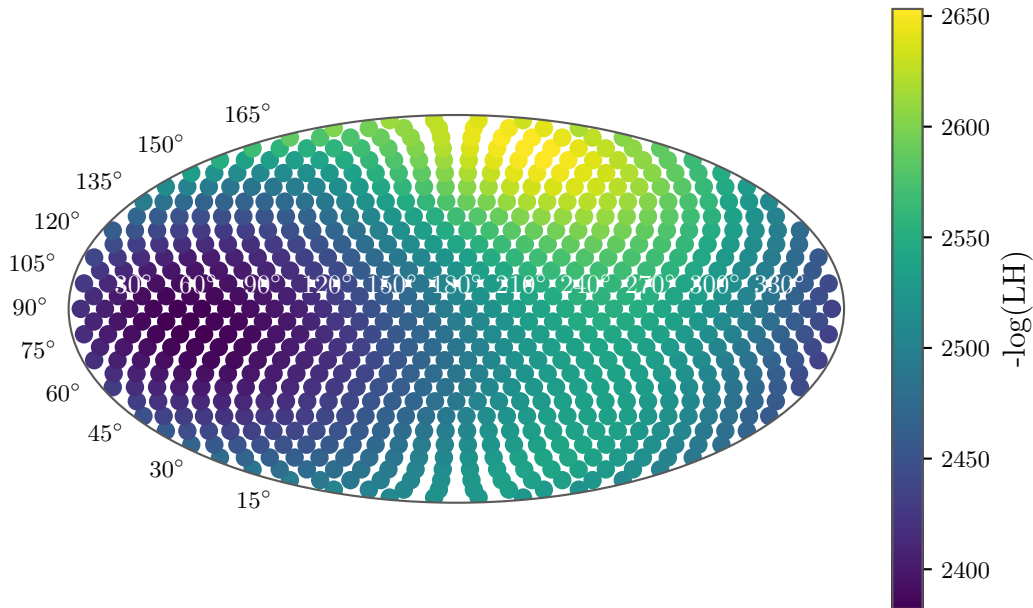


Figure 5.8: Likelihood sky map. Plotted is the $-\log(LH)$ as color of a cascade (run ID: 127225) as a function of θ ($0 - 180^\circ$) and ϕ ($0 - 360^\circ$).

where the minimum in $-\log(LH)$ is located.

Next, only the region of the sky around the minimum is scanned in more detail. The feature to select certain angles has been added to the existing reconstruction. A different, yet more conclusive way of visualizing the data is to plot the $-\log(LH)$ versus the two angles, θ (zenith, $0-180^\circ$) and ϕ (azimuth, $0-360^\circ$) separately which is shown in figure 5.9. Different values of likelihood for one specific θ result from different ϕ belonging

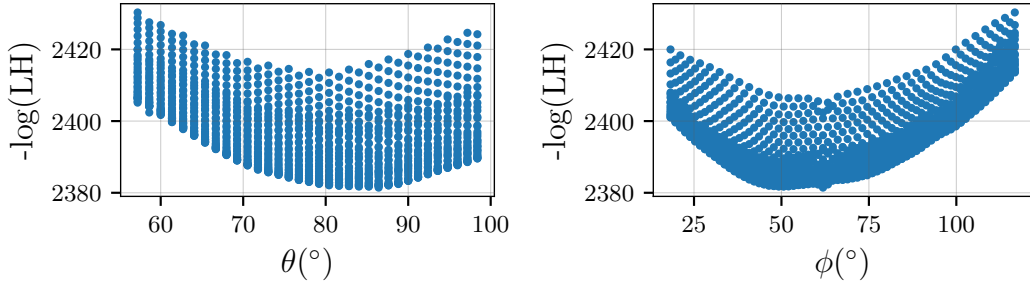


Figure 5.9: Likelihood displayed separately for each angle of the same event; zenith direction left, azimuth right for a selected region around the minimum.

to the same pair of coordinates. Since not all distributions are smooth enough at the lower edge simply reading out the minimum of the data is not sufficiently accurate.

Therefore, in a third and last step only one angle is varied while the other is fixed at the previously determined best fit value. This gives a curve such as in figure 5.10 where the azimuth angle was fixed. A fit with an eighth-degree polynomial results in a function smooth enough to read out the minimum with high precision. Not always is the likelihood function symmetric around its minimum and it can also have features like bumps further away from it which demands such a high-ordered polynomial to fit the curve decently. Selecting a small region around the minimum and fitting a second-ordered polynomial yielded worse fit results on average.

Having an analytic function also helps to calculate the uncertainties as the angle belonging to the specific likelihood limit is now unambiguous. The azimuth angle is treated the same way, shown in figure 5.11.

The fixed angle is close to, but not exactly the minimum as it was determined in the second step. This, however, has not much of an impact as the behavior of the varied angle is very similar for different fixed angles close to the minimum. In other words: If the fixed angle is slightly off, the shape and most importantly the position of the minimum of the likelihood function would still be the same.

The more direct approach of simply taking the minimum of this data

proved to be more inaccurate. This became apparent when the results already available in the collaboration were compared to a re-analysis using the same standard pulses but sparser binning. Differences were smaller when using the fit method described above.

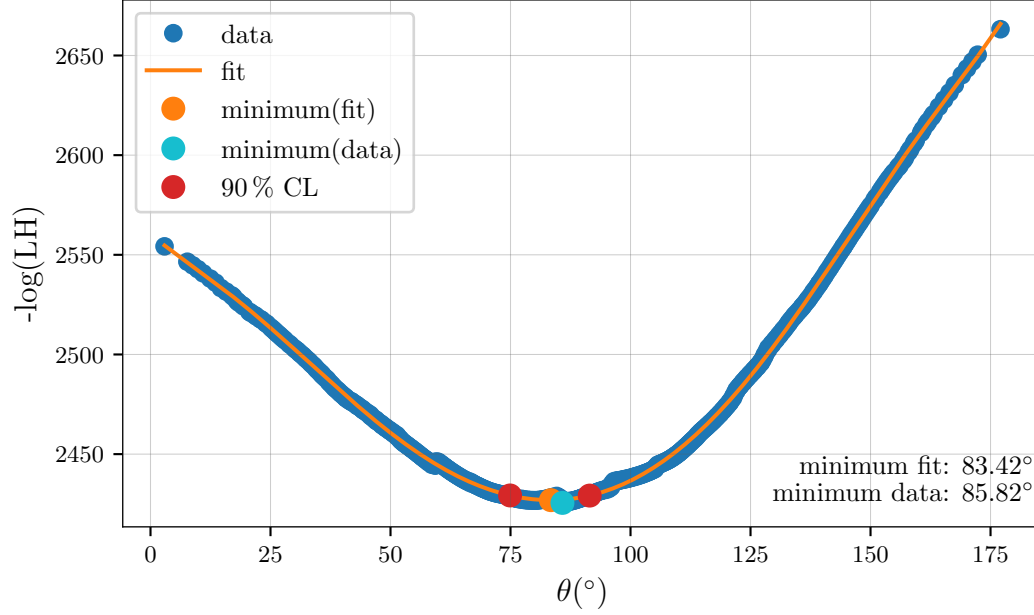


Figure 5.10: The likelihood $-\log(LH)$ as a function of the zenith angle with fixed azimuth angle. The minimum of the fit function is taken for further studies as is the limit for 90 %CL. For comparison the minimum of the data is also drawn.

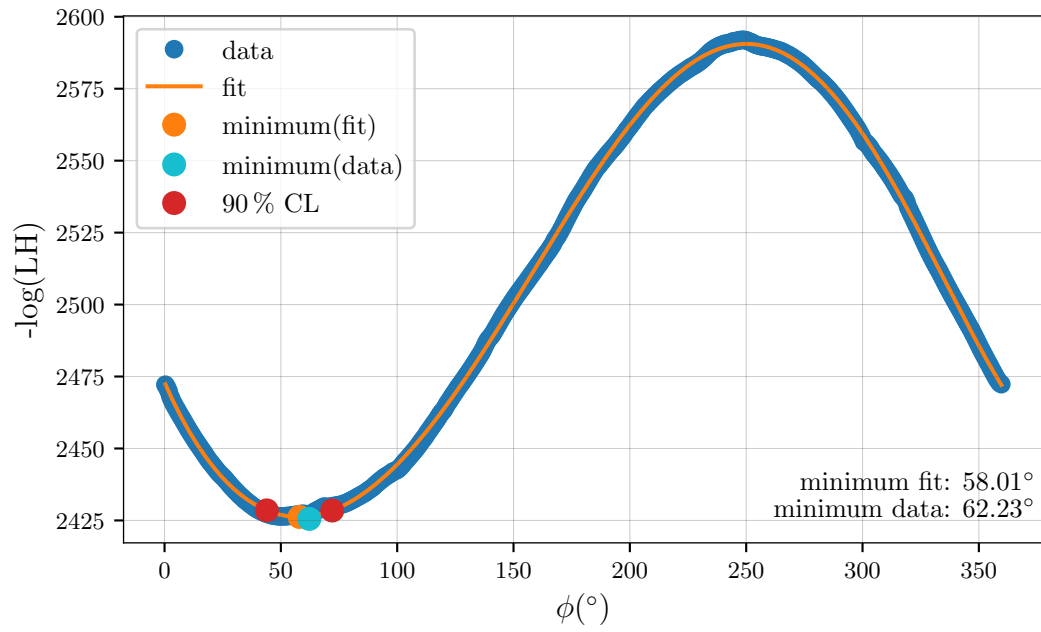


Figure 5.11: Likelihood as a function of the azimuth angle with fixed zenith angle.

5.2.3 Results and evaluation

In order to determine which setup yields more accurate results in the direction reconstruction, it is intuitively instructive to compare the obtained coordinates to the ones from the standard reconstruction. If done so the data shows significant deviations between the two samples. One reason for this could be the fact that the waveform of the fADC is not considered for ToT pulses as it was the case for the standard pulses. Since the reference setup of 600 thresholds has already established itself as a reliable quality measure it will be used again for comparison to decide which one of the other setups, exponential, semi-exponential and linear, performs best. To give an impression of how far off the reconstructed directions were compared to the standard data, the difference from the reference to the standard reconstruction is also given in the following plots.

In order to get directions in the standard case, the analyzed data was already available with extremely fine binning of the likelihood sky map. Therefore the above-described procedure is cut short to the last step of fitting a function to the lower edge of the $-\log(LH)$ for each angle. Note that the data spans the whole sky and thus contains many values of

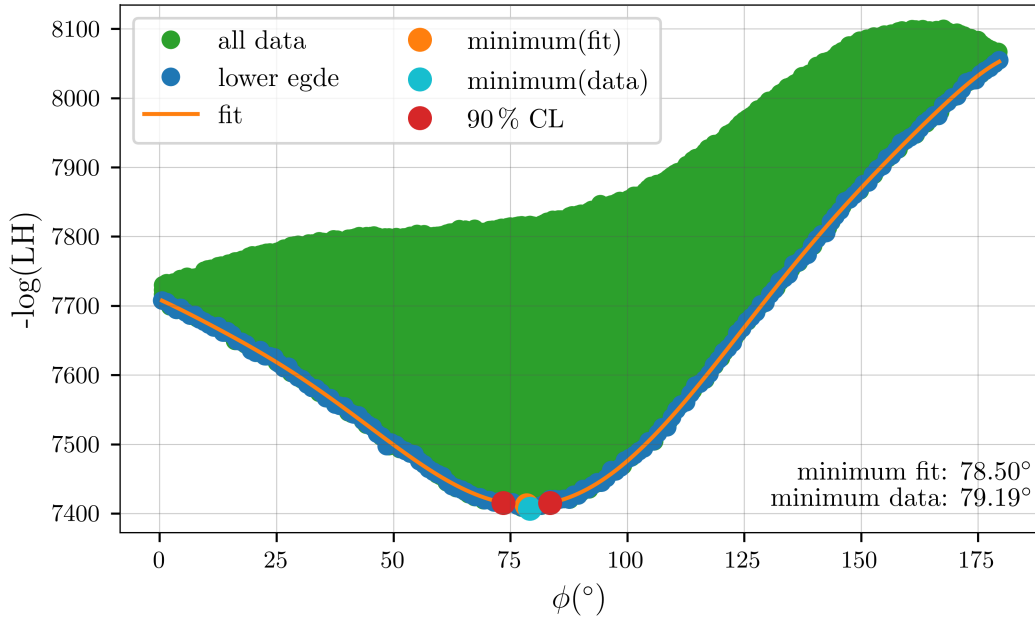


Figure 5.12: Likelihood of standard reconstruction data versus zenith angle. The lower edge (blue) was selected from all data (green) to fit a function and determine the minimum.

likelihoods for one specific angle as the other angle is varied like it was the

case in figure 5.9. Therefore the lowest points had to be selected first. This selection is then fitted and the uncertainties are calculated as described before. Figure 5.12 pictures the procedure for the zenith angle.

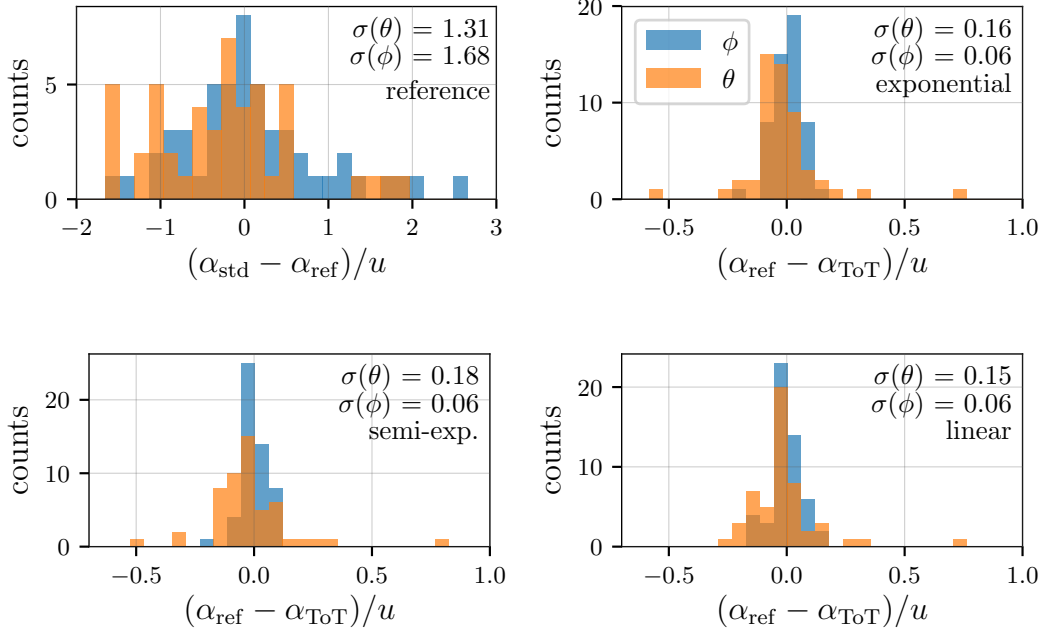


Figure 5.13: Difference in reconstructed directions for each angle separately normalized to the uncertainty. Top left: Results from reference setup to standard reconstruction. Top right: Exponential distribution compared to reference. Bottom left: Semi-exponential setup compared to reference. Bottom right: Linear compared to reference setup.

Considering the results of the reconstruction from all four setups, the first step is to check for systematic effects that occur in either of the angular directions. For each processed cascade event the difference between expected and measured angle in zenith and azimuth is taken and divided by the uncertainty of the expected one. This accounts for the fact that events differ in how accurately they can be reconstructed and thus having different uncertainties. Normalizing the found difference like that allows for better comparability between events.

In figure 5.13, top left, the expected angles are θ and ϕ of the standard reconstruction (α_{std}), and the measured ones are taken from the reference setup of ToT pulses (α_{ref}). As mentioned, this is only shown to motivate why the other setups are not compared to the standard data: Observed can be a difference of up to two times as large as the uncertainty leaving

no possibility for a meaningful conclusion. The difference also stems from the fact that further steps have been performed in the case of the standard reconstruction that are not included in the scope of this thesis.

For the other three plots in this figure the setup in question (α_{ToT}) is set off against the reference (α_{ref}). No significant deviation from a normal distribution around zero is observable. In general, the directions obtained with ToT pules are consistent with each other as they show similar distributions and features for both θ and ϕ equally. One event having an offset of about 0.75 is, for example, present in all three cases. Also, the reconstruction in azimuth direction is predominantly more accurate. This is primarily due to the larger uncertainties assumed for ϕ .

To find a distinct measure for determining how far away the reconstructed directions are apart from each other the direct angle between them is calculated. The angle $\Delta\alpha$ between two vectors \vec{u} and \vec{v} is given by the relation

$$\cos \Delta\alpha = \frac{\vec{u} \cdot \vec{v}}{|\vec{u}| \cdot |\vec{v}|}.$$

The vectors in our case are given in spherical coordinates (with $r = 1$), so $\vec{u} = (u_1, u_2, u_3) = (\sin \theta \cos \phi, \sin \theta \sin \phi, \cos \theta)$. Writing everything out and using trigonometric relations the angle $\Delta\alpha$ simplifies to

$$\Delta\alpha = \arccos(\cos \theta_u \cos \theta_v + \sin \theta_u \sin \theta_v \cos(\phi_u - \phi_v)).$$

The quantity $\Delta\alpha$ is plotted in figure 5.14 which consists of the same four cases as in the previous figure.

The mean values of the entries in the histogram characterize the performance of each setup. The huge mean value when comparing the standard data and reference setup of 26° has been discussed. For the other cases, the overview of figure 5.15, left, has the weighted means plotted. That includes that, while calculating the mean, each entry is weighted by the combined uncertainty from zenith and azimuth direction. The uncertainty in this plot is given by the standard deviation of the fit. Note that there is no systematic uncertainty included arising, for example, from the method used to read out the maxima in the likelihood space.

The ranking shows that the linear setup is slightly favored when it comes to direction reconstruction. However, not significantly, as the one σ limits of exponential and semi-exponential distributions intersect with the one from the linear setup. The fact that the results from the different setups do not differ by much is to be expected; Concluding from figure 5.6 they showed no considerable difference in their respective time reconstruction in relation to time scales of several hundred nano seconds that lie between two hits on different DOMs. Furthermore, the linear setup proved to perform better in charge reconstruction for larger waveforms which are important in the direction reconstruction. This importance is underlined by the difference in direction between standard results and the used reference;

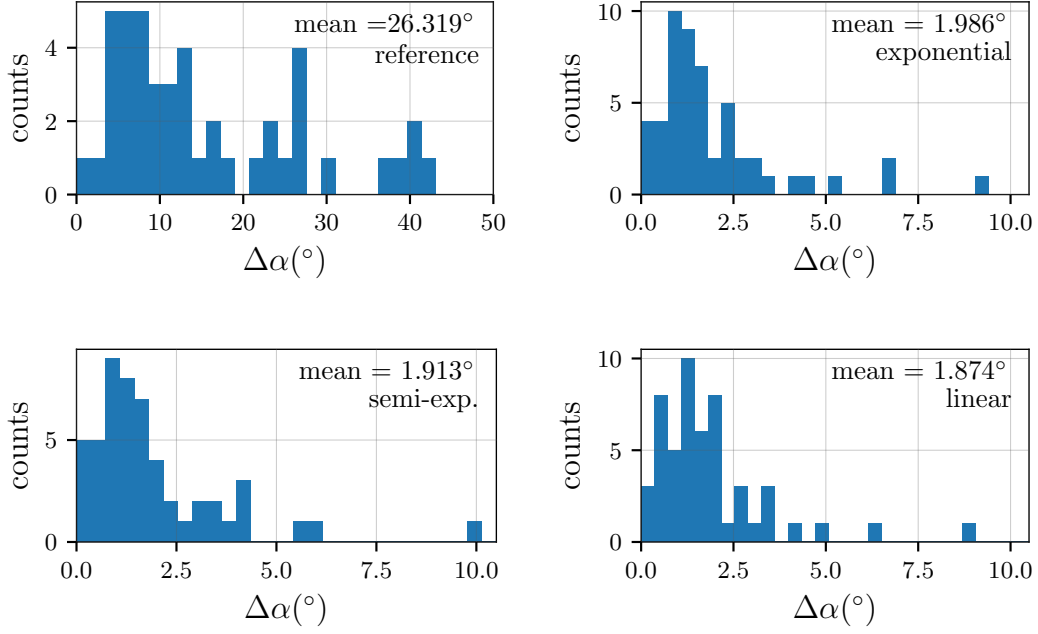


Figure 5.14: Histogram of the direct angle between the compared directions. Top left: Reference to standard. Top right: Exponential to reference. Bottom left: Semi-exponential to reference. Bottom right: Linear to reference.

in the second case the fADC signal is not considered which holds further information about large, long-lasting, and saturated waveforms.

The absolute values of less than 2° prove consistency between the studied setups with, however, the semi-exponential distribution performing out of line. This indicates that there are other factors playing a part that are not directly apparent.

On the right of figure 5.15 the normalized angles are taken and compared following the idea behind figure 5.13. The ordinate axis gives the ratio of the difference in direction to the combined uncertainty. Observable are values between 12 and 13%, with the same remarks valid as in the case of a weighted mean concerning ranking and spread. The uncertainty in this case is given by the standard error on the mean value of the distribution.

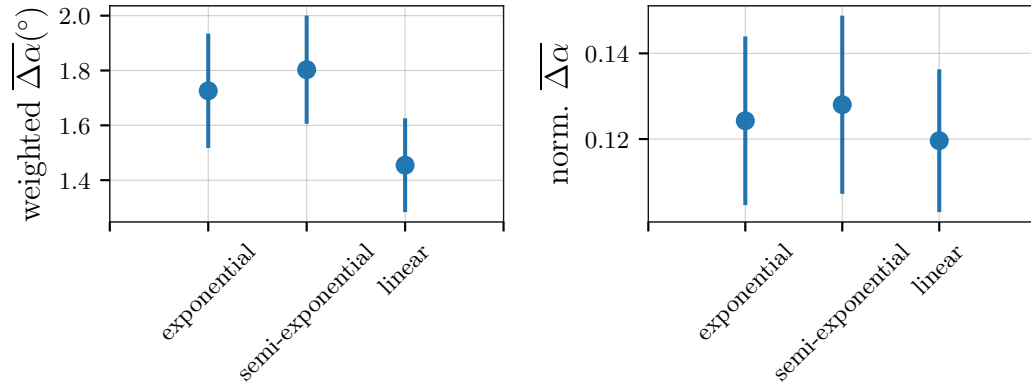


Figure 5.15: Comparison of the performances in direction reconstruction from the studied setups. The mean of $\Delta\alpha$ from all events gives the concluding result.

Summary and outlook

IN this thesis detailed studies conducted on a time-over-threshold readout for the mDOM to be used in a future IceCube extension were presented. They were based on the approach of simulating the sampling of a waveform and the subsequent deconvolution of the incident pulses. Based on these results, optimized setups for threshold positions have been determined.

The studies proved to be challenging in two ways: First, finding sound parameters characterizing well-performing setups including a method to distinctly identify them. And second: Proving reliability and consistency of the results without the opportunity to compare them to any similar works.

After motivating the need for a ToT readout due to the limitations on the power budget of the mDOM, the programs used were introduced. The algorithm to sample a waveform using (several) amplitude thresholds and time-stamping the crossing of the signal has been explained. In conjunction with this, deconvolution of the detected signal from the module's response has been presented. Using this knowledge and the programs mentioned, the studies concentrated on two different aspects: The investigation of single photoelectron pulses and the determination of optimal positions for thresholds covering that region, using generated waveforms. Furthermore the whole dynamic range was examined and different setups were tested. This time, IceCube data was used as input and direction reconstruction was performed.

The presented work included a method that was employed to search for setups yielding the most accurate reconstruction utilizing the parameters representing time and charge, Δt and ΔQ . From that, the optimal threshold positions were deduced. For all considered cases, a distinct optimum was found proving to be in accordance with the parameter χ^2 exhibiting similarity between input and reconstructed waveform. It became apparent that for several thresholds involved, their distribution tends towards being evenly spaced with a maximum at around 1.2 pe. The case of a single threshold was also presented exhibiting an optimal position at 0.21 pe.

Analyzing the waveforms of the HESE dataset, the quality parameters were evaluated for different total charge contained in the ATWD's signal. Three setups, namely exponential, semi-exponential and linear have been compared. The results revealed a more precise reconstruction of the charge

in smaller waveforms up to 80 pe by the exponential setup. Beyond that region, the denser thresholds towards the upper end of the dynamic range favored the linear distribution. The study of the time reconstruction revealed no significant differences between the considered setups. Following that, the principle of direction reconstruction in IceCube has been outlined including how uncertainties are defined for the incident angle in the likelihood space. The procedure to determine the direction from the data used in this thesis has been shown and results were presented. Due to the similar behavior in the time reconstruction and its importance to direction reconstruction no definite favorite setup could be determined in this case. Results proved to be consistent when comparing the studied setups among each other including a reference setup.

Considering all results achieved with this thesis a choice has to be made whether precise reconstruction of small or large waveforms is preferred. Quantitative estimates have been set as indicators to decide what physics are most important to the future extensions to IceCube experiment.

Further reaching studies should be conducted on the treatment of the time reconstruction. In both generated and real data effects had to be explained or circumvented. In order to exclude the systematic effects found in the single photoelectron studies a parameterization could be invented or modifications to the algorithm could be implemented.

If the actual experimental realization is decided on specifications like the number of thresholds or the sampling window width can be fixed in the simulation and more extensive investigations including the simulation of larger waveforms can be launched.

Since a prototype of the mDOM is planned to be finished by the end of 2018, the time-over-threshold readout can be tested in situ for the first time.

Moreover, the KM3NeT experiment will finish deployment in the Mediterranean soon and will serve as a role model of an actively operating experiment utilizing the same readout principle. This offers the possibility to gain valuable experience, not only for construction and development but also for analysis techniques.

Bibliography

- [1] T. Mayer-Kuckuk, *Kernphysik*, Teubner, 2002.
- [2] G. Aad, et al. (ATLAS Collaboration), *Observation of a new particle in the search for the Standard Model Higgs boson with the ATLAS detector at the LHC*, Phys. Lett. B716 (2012) 1–29, Preprint 1207.7214.
- [3] W. Pauli, *On the earlier and more recent history of the neutrino (1957)*, Neutrino Physics, Cambridge Univ. Press.
- [4] C. L. Cowan, et al., *Detection of the free neutrino: a confirmation*, Science 124 (3212) (1956) 103–104. URL <http://science.sciencemag.org/content/124/3212/103>
- [5] Y. Fukuda, et al. (Super-Kamiokande Collaboration Collaboration), *Evidence for oscillation of atmospheric neutrinos*, Phys. Rev. Lett. 81 (1998) 1562–1567. URL <https://link.aps.org/doi/10.1103/PhysRevLett.81.1562>
- [6] G. A. McGregor (SNO Collaboration), *First results from the Sudbury Neutrino Observatory*, in: Proceedings, 37th Rencontres de Moriond on Electroweak Interactions and Unified Theories: Les Arcs, France, March 9-16, 2002, 2002, pp. 249–256, Preprint nucl-ex/0205006. URL https://inspirehep.net/record/586804/files/Pages_from_C02-03-09_249.pdf
- [7] J. Wolf, et al., *The KATRIN neutrino mass experiment*, Nuclear Instruments and Methods in Physics Research Section A: Accelerators, Spectrometers, Detectors and Associated Equipment 623 (1) (2010) 442–444. URL <https://doi.org/10.1016/j.nima.2010.03.030>
- [8] G. F. Smoot, *COBE observations and results*, in: Conference on 3K cosmology, ASCE, 1999. URL <https://doi.org/10.1063/1.59326>
- [9] P. D’Avanzo, *Short gamma-ray bursts: A review*, Journal of High Energy Astrophysics 7 (2015) 73 – 80, swift 10 Years of Discovery, a novel approach to Time Domain Astronomy. URL <http://www.sciencedirect.com/science/article/pii/S2214404815000415>
- [10] U. Schwanke (H.E.S.S. Collaboration), *Status of the HESS experi-*

- ment, eConf C030626 (2003) FRAP16, Preprint astro-ph/0307287, [,387(2003)].
- [11] P. Blasi, *The origin of galactic cosmic rays*, The Astronomy and Astrophysics Review 21 (1). URL <https://doi.org/10.1007/s00159-013-0070-7>
 - [12] L. Mohrmann, *Characterizing cosmic neutrino sources*, Ph.D. thesis, Humboldt-Universität zu Berlin, Mathematisch-Naturwissenschaftliche Fakultät (2015).
 - [13] B. P. Abbott, et al. (LIGO Scientific Collaboration and Virgo Collaboration Collaboration), *Gw170817: Observation of gravitational waves from a binary neutron star inspiral*, Phys. Rev. Lett. 119 (2017) 161101. URL <https://link.aps.org/doi/10.1103/PhysRevLett.119.161101>
 - [14] U. Katz, C. Spiering, *High-energy neutrino astrophysics: Status and perspectives*, Progress in Particle and Nuclear Physics 67 (3) (2012) 651–704. URL <https://doi.org/10.1016/j.pnpnp.2011.12.001>
 - [15] M. G. Baring, *Diffusive shock acceleration: The Fermi mechanism*, in: Very high-energy phenomena in the universe. Proceedings, 32nd Rencontres de Moriond, Les Arcs, France, January 18-25, 1997, 1997, pp. 97–106, Preprint astro-ph/9711177. URL https://inspirehep.net/record/452485/files/C97-01-18_97-106.pdf
 - [16] C. Grupen, *Astroparticle Physics*, Springer, 2005.
 - [17] P. Mészáros, *Gamma-ray bursts*, Reports on Progress in Physics 69 (8) (2006) 2259. URL <http://stacks.iop.org/0034-4885/69/i=8/a=R01>
 - [18] H. Krawczynski, E. Treister, *Active Galactic Nuclei - the Physics of Individual Sources and the Cosmic History of Formation and Evolution*, Front. Phys.(Beijing) 8 (2013) 609–629, Preprint 1301.4179.
 - [19] K. S. Long, et al. (ASTRO-H Science WorkiG Group Collaboration), *ASTRO-H White Paper - Older Supernova Remnants and Pulsar Wind Nebulae*, ASTRO-H Space X-ray Observatory White Paper Preprint 1412.1166.
 - [20] E. Waxman, J. Bahcall, *High energy neutrinos from astrophysical sources: An upper bound*, Physical Review D 59 (2). URL <https://doi.org/10.1103/physrevd.59.023002>
 - [21] J. A. Formaggio, et al., *From eV to EeV: Neutrino cross sections across energy scales*, Reviews of Modern Physics 84 (3) (2012) 1307–1341. URL <https://doi.org/10.1103/revmodphys.84.1307>

-
- [22] L. Classen, *Prototyping a novel optical module for the iccube-gen2 neutrino telescope*, Ph.D. thesis, Friedrich-Alexander-Universität Erlangen-Nürnberg (2017). URL https://www.uni-muenster.de/imperia/md/content/physik_kp/agkappes/abschlussarbeiten/doktorarbeiten/1702-phd_lclassen.pdf
- [23] M. Aartsen, et al., *The IceCube neutrino observatory: instrumentation and online systems*, Journal of Instrumentation 12 (03) (2017) P03012–P03012. URL <https://doi.org/10.1088/1748-0221/12/03/p03012>
- [24] P. A. Cherenkov, *Visible emission of clean liquids by action of γ radiation*, Doklady Akademii Nauk SSSR 2 (1934) 451+. URL <http://ufn.ru/en/articles/2007/4/g/>
- [25] R. Abbasi, et al., *The design and performance of IceCube DeepCore*, Astroparticle Physics 35 (10) (2012) 615–624. URL <https://doi.org/10.1016/j.astropartphys.2012.01.004>
- [26] R. Abbasi, et al., *IceTop: The surface component of IceCube*, Nuclear Instruments and Methods in Physics Research Section A: Accelerators, Spectrometers, Detectors and Associated Equipment 700 (2013) 188–220. URL <https://doi.org/10.1016/j.nima.2012.10.067>
- [27] W. R. Leo, *Techniques for Nuclear and Particle Physics Experiments*, Springer, 1994.
- [28] C. Kopper (Ed.), *Observation of Astrophysical Neutrinos in Six Years of IceCube Data*, Proceedings of Science, 2017.
- [29] A. Stoessl (Ed.), *Muon track reconstruction and veto performance with D-Egg sensor for IceCube-Gen2*, Proceedings of Science, 2017.
- [30] M. G. Aartsen, et al. (IceCube Collaboration), *IceCube-Gen2: A Vision for the Future of Neutrino Astronomy in Antarctica*, PoS FRAPWS2016 (2017) 004, Preprint 1412.5106.
- [31] M. G. Aartsen, et al. (IceCube PINGU Collaboration), *Letter of Intent: The Precision IceCube Next Generation Upgrade (PINGU)* Preprint 1401.2046.
- [32] A. Margiotta (KM3NeT Collaboration), *The KM3NeT deep-sea neutrino telescope*, Nucl. Instrum. Meth. A766 (2014) 83–87, Preprint 1408.1392.
- [33] P. Timmer, E. Heine, H. Peek, *Very low power, high voltage base for a photo multiplier tube for the km3net deep sea neutrino telescope*, Journal of Instrumentation 5 (12) (2010) C12049. URL <http://stacks.iop.org/1748-0221/5/i=12/a=C12049>
- [34] F. Gonnella, V. Kozhuharov, M. Raggi, *Time over threshold in*

- the presence of noise*, Nucl. Instrum. Meth. A791 (2015) 16–21, Preprint 1412.1743.
- [35] *Icecube documentation: Ictray*, <http://software.icecube.wisc.edu/documentation/projects/icetray/index.html>, accessed: 14.01.2018.
- [36] C. L. Lawson, R. J. Hanson, *Solving least squares problems*, Prentice-Hall Series in Automatic Computation, Englewood Cliffs: Prentice-Hall, 1974.
- [37] *Icecube documentation: I3wavedeform*, <http://software.icecube.wisc.edu/documentation/projects/wavedeform/index.html>, accessed: 22.11.2017.
- [38] M. Dittmer, Personal communication, 12.07.2017.
- [39] *Data sheet photomultiplier tube r12199*, https://www.hamamatsu.com/resources/pdf/etd/R12199_TPMH1356E.pdf, accessed: 12.12.2017.
- [40] K. M. Gorski, et al., *HEALPix: A framework for high-resolution discretization and fast analysis of data distributed on the sphere*, The Astrophysical Journal 622 (2) (2005) 759–771. URL <https://doi.org/10.1086/427976>
- [41] S. S. Wilks, *The large-sample distribution of the likelihood ratio for testing composite hypotheses*, Ann. Math. Statist. 9 (1) (1938) 60–62. URL <https://doi.org/10.1214/aoms/1177732360>

Acknowledgements

I would like to thank very much Prof. Dr. Alexander Kappes for giving me the opportunity to do my Master's thesis under his supervision. Not only was he always there to help me advance, especially at the beginning, but also the climate he creates as the group's head is very friendly and cooperative.

Further, thanks to Dr. Volker Hannen for taking over (again) as the second corrector.

I was able to get to know a few members of the IceCube collaboration (most of them over the internet advising me on the IceTray software) and was happy to see that everyone "is so nice". Especially Claudio Kopper helped me a lot with his reconstruction and answered my statistics questions even at the strangest hours.

Dr. Lew Classen also needs to be thanked for he is chronically in a good temper and also knows quite a lot about anything making him the victim of many of my questions.

The rest of the group is also kind of ok. I mean, sure, there are quite a few Spanish speaking Spaniards, two people using the same name to cause confusion, and even a girl - eugh! Gladly, another one of that kind fled as far away as possible stranding on the surreal continent of Antarctica. I am also happy that we had two hard working bachelors during my time and that they are gone now.

Other than that, I was quite happy being in this working group and enjoyed every moment, making this the best time of my years of study ♡. Most of the time most of you even got my humor!

I am blessed to be part of Random People Productions, responsible for many viral YouTube videos about physics, like "Unboxing Random Stuff: Tennis Racket" or "Unboxing Inverse - A Live Art Performance". All that would not have been possible without the quality content each one of you provided.

I also would like to thank my parents. Without them I would not have made it this far. In fact, I would have died right away as I wasn't able to get something to drink and to eat for myself as a newborn baby.

Declaration

I, Daniel Guderian, declare that this thesis titled, “Performance and optimization studies on the time-over-threshold readout of the multi-PMT optical module for future IceCube extensions” and the work presented in it are my own. I confirm that:

- This work was done wholly or mainly while in candidature for a research degree at this University.
- Where any part of this thesis has previously been submitted for a degree or any other qualification at this University or any other institution, this has been clearly stated.
- Where I have consulted the published work of others, this is always clearly attributed.
- Where I have quoted from the work of others, the source is always given. With the exception of such quotations, this thesis is entirely my own work.
- I have acknowledged all main sources of help.
- Where the thesis is based on work done by myself jointly with others, I have made clear exactly what was done by others and what I have contributed myself.

Münster,
